

## RESEARCH ARTICLE

10.1002/2014JD021912

## Key Points:

- Sensitivity of simulated tropical sea breeze convection is investigated
- Enhanced aerosols and reduced soil moisture each individually reduce rainfall
- Nonlinear aerosol-cloud-land surface system response can enhance rainfall

## Correspondence to:

L. D. Grant,  
ldgrant@atmos.colostate.edu

## Citation:

Grant, L. D., and S. C. van den Heever (2014), Aerosol-cloud-land surface interactions within tropical sea breeze convection, *J. Geophys. Res. Atmos.*, 119, 8340–8361, doi:10.1002/2014JD021912.

Received 17 APR 2014

Accepted 16 JUN 2014

Accepted article online 19 JUN 2014

Published online 12 JUL 2014

## Aerosol-cloud-land surface interactions within tropical sea breeze convection

Leah D. Grant<sup>1</sup> and Susan C. van den Heever<sup>1</sup><sup>1</sup>Department of Atmospheric Science, Colorado State University, Fort Collins, Colorado, USA

**Abstract** In this study, the influence of aerosols, surface roughness length, soil moisture, and synergistic interactions among these factors on tropical convective rainfall focused along a sea breeze front are explored within idealized cloud-resolving modeling simulations using the Regional Atmospheric Modeling System (RAMS). The idealized RAMS domain setup is representative of the coastal Cameroon rainforest in equatorial Africa. In order to assess the potential sensitivity of sea breeze convection to increasing anthropogenic activity and deforestation occurring in such regions, 27 total simulations are performed in which combinations of enhanced aerosol concentrations, reduced surface roughness length, and reduced soil moisture are included. Both enhanced aerosols and reduced soil moisture are found to individually reduce the precipitation due to reductions in downwelling shortwave radiation and surface latent heat fluxes, respectively, while perturbations to the roughness length do not have a large impact on the precipitation. The largest soil moisture perturbations dominate the precipitation changes due to reduced low-level moisture available to the convection, but if the soil moisture perturbation is more moderate, synergistic interactions between soil moisture and aerosols enhance the sea breeze precipitation. This is found to result from evening convection that forms ahead of the sea breeze only when both effects are present. Interactions between the resulting gust fronts and the sea breeze front locally enhance convergence and therefore the rainfall. The results of this study underscore the importance of considering the aerosol-cloud-land surface system responses to perturbations in aerosol loading and land surface characteristics.

### 1. Introduction

Some of the highest global annual rainfall totals on the order of 2–3 m yr<sup>-1</sup> [Liebmann *et al.*, 2012] are found in the equatorial rainforest regions of Africa, Amazonia, and Indonesia where tropical convection occurs year round. It is well known that convection in these regions plays a crucial role in the global circulation through its impacts on the ascending branch of the Hadley Cell [Riehl and Malkus, 1958] and on the global hydrological cycle [Avissar and Werth, 2005]. However, these regions are under ever increasing anthropogenic activity, including biomass burning and deforestation practices. Such anthropogenic activity may have significant impacts on the convective storm characteristics and rainfall patterns in these critical tropical rainforest regions through aspects such as changing land surface properties and atmospheric aerosol loading [e.g., Andreae *et al.*, 2004; Ramos da Silva and Avissar, 2006; Koren *et al.*, 2008]. It is therefore highly important to understand the response of convective storms to these anthropogenic factors if we are to understand the impacts of increasing human populations on tropical convection, tropical rainfall, and the large-scale circulation.

Convection in Africa is anomalous relative to the other equatorial land regions such as Amazonia and Indonesia [e.g., Mohr and Zipser, 1996a, 1996b; Mohr *et al.*, 1999; Petersen and Rutledge, 1998, 2001; McCollum *et al.*, 2000]. While annual rainfall in equatorial Africa is comparatively lower, convection is more intense by measures such as high (40 dBZ) reflectivity echo top height, minimum brightness temperature, and lightning flash rate [Zipser *et al.*, 2006]. Mesoscale convective systems (MCSs) are also disproportionately larger in equatorial Africa [Nesbitt *et al.*, 2006]. The reasons for these differences are not well understood, as there have been comparatively fewer studies of equatorial African convection than in other tropical rainforest regions. This study therefore focuses on tropical convection over Africa. Rainfall patterns over equatorial Africa are also highly spatially variable [Balas *et al.*, 2007]. Part of this variability is likely a result of mesoscale-organized convection that is modulated by both larger- and smaller-scale features including the Madden-Julian Oscillation, midlevel easterly jets, convectively coupled Kelvin waves, topography, and sea and lake breezes [Laing *et al.*, 2011; Jackson *et al.*, 2009].

The sea breeze represents a persistent forcing mechanism for deep convection and rainfall. Its importance, particularly in the diurnal cycle of rainfall, has been noted in several studies of deep convection in the tropics [Yang and Slingo, 2001; Nesbitt and Zipser, 2003; Kikuchi and Wang, 2008], as well as in equatorial Africa [Laing et al., 2008, 2011]. Many studies have demonstrated the sensitivity of the sea breeze structure, local convergence, and resulting precipitation to various processes and mechanisms including sensible heat fluxes, soil moisture, surface roughness length, coastline curvature, and interaction with existing boundaries such as land breezes, other sea breezes, and gust fronts [Wakimoto and Atkins, 1994; Atkins et al., 1995; Kingsmill, 1995; Fankhauser et al., 1995; Wilson and Megenhardt, 1997; Carbone et al., 2000; Baker et al., 2001; Fovell and Dailey, 2001; Marshall et al., 2004; Fovell, 2005; Crosman and Horel, 2010, and references therein]. Sea breeze-generated precipitation may also be sensitive to changes in aerosol concentrations through aerosol direct effects and indirect effects on the storm dynamics and microphysics [e.g., Andreae et al., 2004; Khain et al., 2005; van den Heever et al., 2006; Koren et al., 2004, 2008; Lin et al., 2006].

While many studies have investigated aerosol-cloud interactions and land-atmosphere interactions separately, very few have considered the synergistic interactions among them within a common analytical framework. The goal of this research is therefore to investigate the potential sensitivity of sea breeze convection over coastal equatorial Africa to changes in aerosol concentrations and land surface characteristics, both independently and synergistically. Such changes to aerosols and the land surface are possible with increasing anthropogenic activity, pollution, and deforestation practices, which are often focused in coastal regions [Hinrichsen, 1999]. Specifically, this study seeks to answer the following questions: (1) What are the mechanisms by which changing aerosol number concentrations, surface roughness length, and soil moisture each individually impact tropical sea breeze precipitation; and (2) how do aerosols interact synergistically with land surface processes to influence the precipitation? These goals are addressed through the use of idealized cloud-resolving modeling simulations.

In this study, it will be demonstrated that the individual impacts of increasing aerosol concentrations and decreasing soil moisture both reduce the sea breeze precipitation, while changes to the surface roughness length only have a slight impact on the precipitation. It will also be shown that the pathway through which aerosols and land surface processes interact synergistically to affect rainfall is through feedbacks to the localized sea breeze convergence by storm-generated gust fronts. The sensitivity of rainfall to these various factors and their interactions is assessed through the analysis of changes to the basic ingredients for deep, moist convection: *moisture, instability, and lift* [e.g., Doswell, 1987; Johns and Doswell, 1992]. Section 2 describes the model configuration, the sensitivity experiments, and the factor separation methodology used for the analysis. The results are presented in section 3, including the mechanisms by which the various processes and their interactions change the sea breeze structure and resulting precipitation. A discussion and conclusions are provided in section 4.

## 2. Experiment Design

### 2.1. RAMS Model Configuration

In this study, idealized simulations were conducted using the Regional Atmospheric Modeling system (RAMS) version 6 [Cotton et al., 2003; Saleeby and van den Heever, 2013]. RAMS is a regional, nonhydrostatic model that is coupled to the Land-Ecosystem-Atmosphere Feedback (LEAF) version 3 land surface parameterization [Walko et al., 2000] and contains a sophisticated microphysics and aerosol parameterization scheme. RAMS is thus an ideal modeling framework with which the goals of this study can be addressed. A summary of the RAMS model configuration is provided in Table 1.

The RAMS simulations presented herein contain a single grid of 550 × 200 km extent, a horizontal grid spacing of 1 km, and 57 vertical levels spanning ~26 km with a minimum vertical grid spacing of 100 m near the surface. The grid resolution is fine enough to explicitly represent deep convection, such as suggested by Ramos da Silva and Avissar [2006] for simulations over the Amazon, and to model the detailed sea breeze structure [Crosman and Horel, 2010] but coarse enough that a large number of sensitivity simulations may be performed within a reasonable time frame. In order to ensure that a vertical grid spacing of 100 m is sufficient in the boundary layer, a sensitivity test with a minimum vertical grid spacing of 50 m was performed for the control simulation. The results from the sensitivity experiment demonstrated that the finer vertical grid spacing did not make a significant difference, as the domain-accumulated precipitation was reduced by only

**Table 1.** RAMS Model Options Used in All of the Sea Breeze Simulations

Model Aspect	Setting
Grid	Arakawa C grid $\Delta x = \Delta y = 1$ km; 550 km $\times$ 200 km domain size $\Delta z$ variable minimum $\Delta z = 100$ m, maximum $\Delta z = 1$ km vertical stretch ratio = 1.05 57 vertical levels; model top $\sim 26$ km
Time integration	3 s time step; 16 h simulation duration
Initialization	Horizontally homogeneous thermodynamic and wind profile, averaged from ECMWF YOTC analysis data Initial start time 600 UTC 1 July Random thermal perturbations through lowest 2 km agl, with a maximum magnitude of 1 K at the lowest model level above ground
Surface scheme	LEAF-3 [Walko et al., 2000] 11 soil levels from 0.01 m to 0.5 m below ground Western third of domain: ocean (SST 300 K) Eastern two thirds of domain: evergreen broadleaf tree surface type, sandy clay loam soil type
Boundary conditions	Radiative lateral boundary [Klemp and Wilhelmson, 1978] in zonal direction; periodic in meridional direction Rayleigh friction damping over top six vertical levels ( $\sim 21$ – $26$ km agl)
Microphysics scheme	Two-moment bulk microphysics [Meyers et al., 1997] 8 hydrometeor classes [Saleeby and Cotton, 2004]
Radiation scheme	Harrington [1997] two-stream, updated every 5 simulation minutes
Aerosol treatment	Aerosol species: sulfates [Saleeby and van den Heever, 2013] No aerosol sources or sinks Aerosols radiatively active
Turbulence scheme	DeMott et al. [2010] ice nucleation parameterization Smagorinsky [1963] deformation K with stability modifications by Hill [1974]; stability modifications by Lilly [1962] used gradually above the boundary layer
Coriolis	No

1.2% and the sea breeze structure and propagation speed were similar. Therefore, the 100 m vertical grid spacing was used for all the experiments performed here. Simulations were run for 16 h, beginning at 700 local time (LT). The Harrington [1997] two-stream radiation scheme was utilized for these experiments.

The RAMS microphysics parameterization is a sophisticated double-moment bulk scheme with bin-emulating procedures for cloud droplet nucleation, riming, and sedimentation. The scheme utilizes a gamma size distribution to represent eight hydrometeor classes, including cloud water, drizzle, rain, pristine ice, snow, aggregates, graupel, and hail. RAMS contains nine possible different aerosol modes for four aerosol particle types, but given the idealized setup of these simulations, only a submicron ammonium sulfate mode was used here. Sulfates are a prevalent aerosol type in the atmosphere, serve as effective cloud condensation nuclei (CCN) due to their high solubility, and are often associated with anthropogenic activity [e.g., Andreae and Rosenfeld, 2008, and references therein]. Aerosol sources and sinks are not included and aerosols are radiatively active in these simulations. Aerosol-radiative interactions are parameterized from Mie calculations in RAMS. The reader is referred to Walko et al. [1995], Meyers et al. [1997], Saleeby and Cotton [2004, 2008], and Saleeby and van den Heever [2013] for further details on the RAMS microphysics scheme and aerosol treatment.

The horizontally homogeneous but vertically varying initial thermodynamic conditions were generated from the European Centre for Medium-Range Weather Forecasts (ECMWF) analyses for the Year of Tropical Convection (YOTC). Temperature, specific humidity, and winds at 600 UTC (700 LT) were averaged spatially from 0°N to 4°N and from 10°E to 20°E, broadly encompassing the Cameroon rainforest region, and temporally from 1 June to 31 August for 2008 and 2009 to create the initial sounding profile for the idealized simulations (Figure 1a). The thermodynamic conditions are therefore representative of one of equatorial Africa's dry seasons, when anthropogenic activity and deforestation practices are more active. Above 300 hPa, the specific humidity was reduced by a factor of 2/3 from the YOTC moisture profile based on the results of Ciesielski et al. [2014], where it was shown that ECMWF moisture analyses are too humid in the upper levels in comparison to high-accuracy, humidity-corrected rawinsonde measurements taken during the Dynamics of the Madden-Julian Oscillation field campaign. Random temperature perturbations were introduced at each

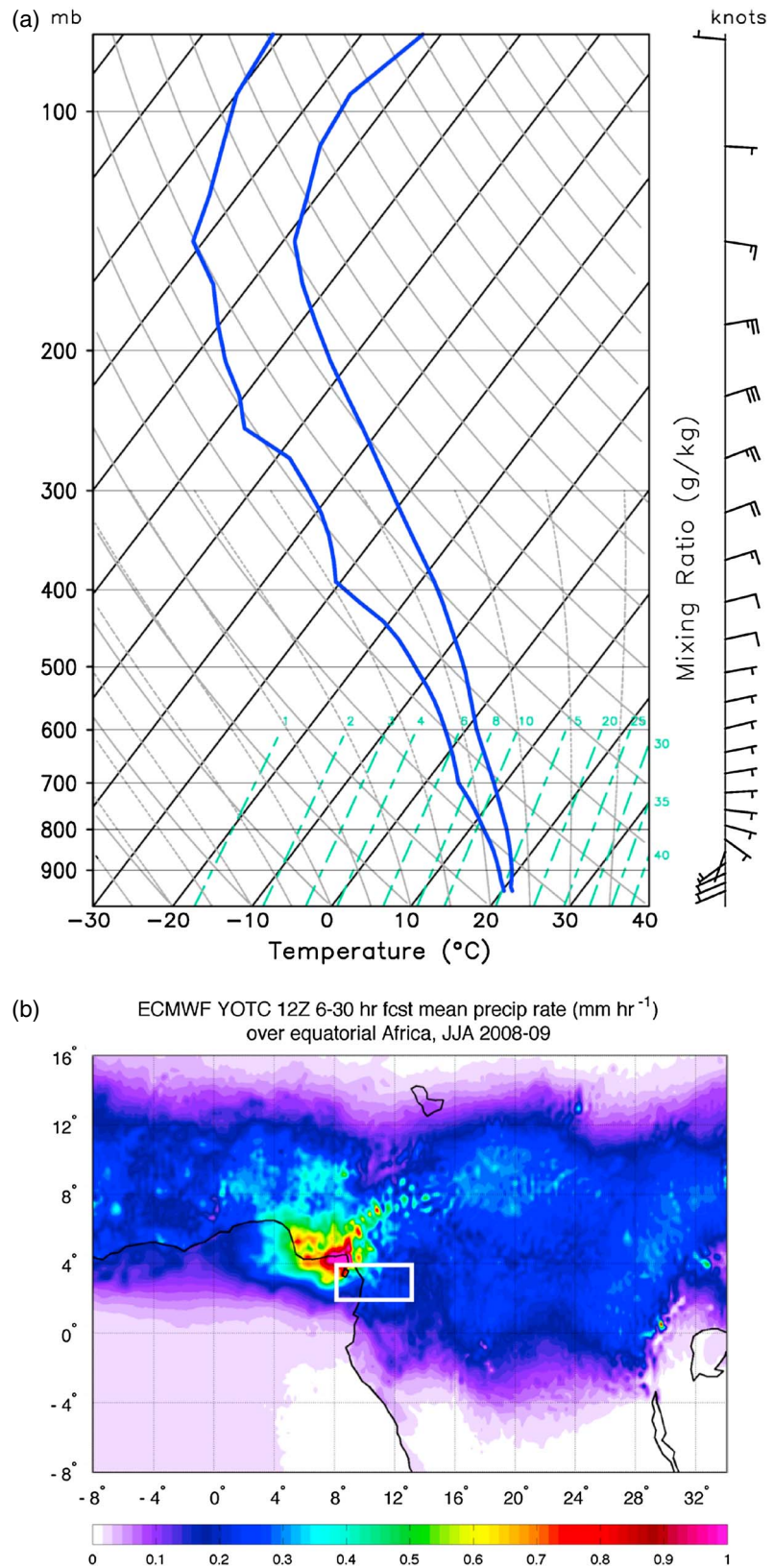


**Figure 1.** (a) Initial thermodynamic temperature and dewpoint sounding, as well as the initial wind profile (barbs, knots), used in all of the idealized simulations. (b) Mean precipitation rate (mm h<sup>-1</sup>) over equatorial Africa, calculated from the ECMWF YOTC forecast data as described in the text. The white box indicates the approximate size of the domain used for the idealized simulations.

grid point within the lowest 2 km above ground level (agl), with a maximum of 1 K at the surface. The random perturbations disrupt the homogeneity of the initial environment and allow the idealized sea breeze to evolve realistically, as will be seen in the analyses of Figures 3 and 4 below.

RAMS is coupled to the LEAF-3 model, an interactive land surface model containing 22 different surface types and 12 soil classes [Walko *et al.*, 2000]. LEAF prognoses temperature and moisture content for multiple soil levels and the vegetation canopy. The land surface and atmosphere can interact through turbulent energy and moisture exchange, radiative transfer, transpiration, and precipitation. Eleven soil levels from 0.01 m to 0.5 m below ground were used in these simulations. The LEAF surface classes chosen for the domain setup are representative of the coastal Cameroon rainforest region: The eastern two thirds of the domain was specified as evergreen broadleaf tree with a sandy clay loam soil type [Rodell *et al.*, 2004] and the western third as ocean with a fixed sea surface temperature (SST) of 300 K, based on the average coastal SST in June, July, and August from the YOTC data set. The approximate domain size and the forest-ocean partition within the domain are indicated in Figure 1b in order to provide a sense of the grid scale. Boundary conditions were open radiative on the east and west sides of the domain but periodic on the north and south sides, so that the simulated domain is representative of an idealized coastline stretching to both the north and south. It should be noted that we are not assessing the impact of coastline curvature on sea breeze convergence and resulting convective precipitation in this study, and hence, we prescribe the imposed ocean-forest border to be perfectly straight. To avoid any potential influence of the model lateral boundary conditions, the region within 50 km of the east and west borders is excluded from the analysis throughout this paper.

## 2.2. Sensitivity Experiments and Analysis Methodology

To address the goals of this study, 27 simulations with varying aerosol concentrations, surface roughness lengths, and soil moisture contents were conducted. It should be noted that the sensitivity of sea breeze precipitation to the initial instability and shear profile, which are known to regulate convective intensity and rainfall accumulation, is not investigated here. For each of the three parameters, two different perturbation values were used from the values chosen in the control (hereafter CTL) simulation: a moderate perturbation and an extreme perturbation. The initial surface aerosol concentration in CTL was  $200 \text{ cm}^{-3}$ . The two perturbation surface values used were  $500 \text{ cm}^{-3}$  and  $2000 \text{ cm}^{-3}$ ; these simulations will be referred to as cMid and cPoll, respectively, where the "c" refers to aerosol particles that can serve as CCN. The CTL surface concentration is representative of clean continental conditions. Similar concentrations have been measured in pristine conditions in Amazonia [Roberts *et al.*, 2001; Gunthe *et al.*, 2009]. The extreme value of  $2000 \text{ cm}^{-3}$  was chosen based on measurements in the Amazon, where aerosol number concentrations of up to  $10,000 \text{ cm}^{-3}$  have been measured near the surface during periods of biomass burning [Martin *et al.*, 2010, and references therein]. In each case, the aerosol number concentration profile was linearly decreased to one tenth of the surface concentration by 4 km agl and was held constant thereafter. The aerosol number concentration profiles for CTL, cMid, and cPoll are displayed in Figure 2a.

The two surface parameters that were varied in these experiments were the roughness length and soil moisture. The initial roughness length in CTL is 3.50 m, which is calculated within the LEAF model from the default evergreen broadleaf class vegetation height of 32 m. The perturbation roughness length values of 1.64 m and 0.22 m were calculated by specifying two perturbation tree heights of 15 m and 2 m, respectively; these simulations will be referred to as tMid and tSml. Soil moisture was initialized horizontally homogeneously by setting the initial soil moisture in CTL to 75% saturated for all soil levels, which corresponds to a soil moisture content of  $0.315 \text{ m}^3 \text{ m}^{-3}$  for the LEAF sandy clay loam soil type. Idealized perturbation soil moisture values were simply specified at 50% saturated and 25% saturated (s50 and s25), corresponding to volumetric soil moisture contents of 0.21 and  $0.105 \text{ m}^3 \text{ m}^{-3}$ , respectively. Similar idealized approaches to soil moisture initialization have also been used in previous studies [Jiang and Feingold, 2006; Gero and Pitman, 2006; Ramos da Silva and Avissar, 2006; Saad *et al.*, 2010]. The range of soil moisture values used here is comparable with the magnitudes of volumetric soil moisture content found along coastal equatorial Africa in June, July, and August within the Global Land Data Assimilation System [Rodell *et al.*, 2004] (available online at [http://gdata1.sci.gsfc.nasa.gov/daac-bin/G3/gui.cgi?instance\\_id=GLDAS10\\_M](http://gdata1.sci.gsfc.nasa.gov/daac-bin/G3/gui.cgi?instance_id=GLDAS10_M)). The initial roughness length and soil moisture for CTL and the sensitivity experiments are depicted in Figures 2b and 2c. The CTL simulation is therefore the least polluted simulation with the wettest soil and the highest surface roughness length.

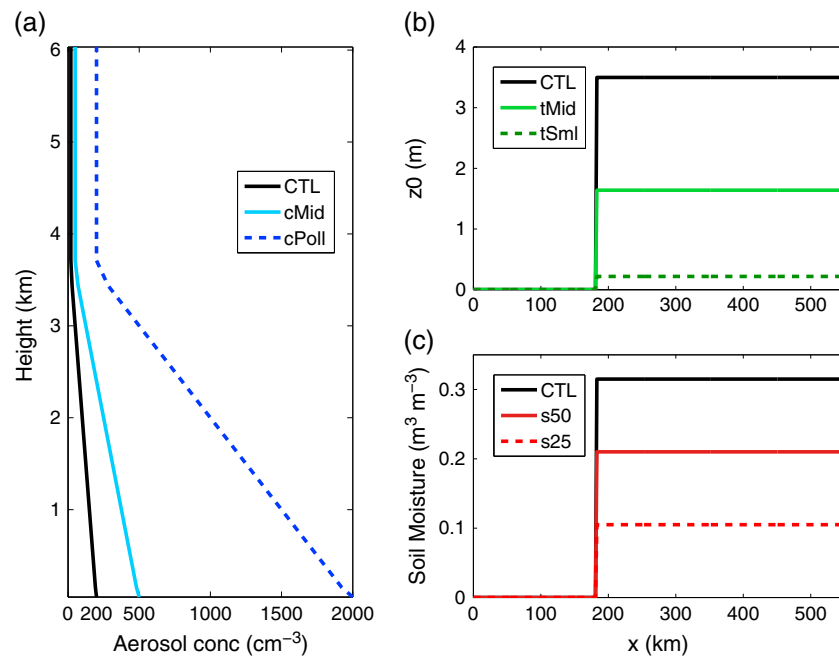


**Figure 2.** Initial conditions for the control simulation (CTL) and the various sensitivity experiments. (a) Aerosol number concentration profile ( $\text{cm}^{-3}$ ) for CTL and the polluted conditions (cMid and cPoll) used for the sensitivity tests. (b) Surface roughness length (m) as a function of east–west position for CTL and sensitivity experiments tMid and tSml. (c) Volumetric soil moisture content ( $\text{m}^3 \text{m}^{-3}$ ) as a function of east–west position for CTL (75% soil moisture saturation) and for the 50% and 25% saturation sensitivity experiments (s50 and s25). Note that the western third of the domain is ocean.

It should be noted that we have not simply altered the land surface type for the sensitivity experiments, as is sometimes done in studies of deforestation impacts. The reasons for this are threefold. First, in reality, the land surface type is usually not completely altered under deforestation scenarios; often, secondary forest regrowth occurs, and the land surface properties are similar to those of the original forest [O'Brien, 2000; Pielke et al., 2007]. In this scenario, one might expect the most significantly altered surface parameter to be the roughness length due to the smaller tree heights. Second, soil moisture is often substantially altered through land use changes [Pielke et al., 2007 and references therein] and has been shown in numerous studies to have a strong impact on land-atmosphere coupling by virtue of its control over the latent and sensible surface energy flux partition, and thus its influence on surface-driven buoyancy and moisture availability for cloud and precipitation formation [e.g., Yu et al., 2002; Ramos da Silva and Avissar, 2006; Betts, 2007, 2009; Taylor et al., 2012]. Third, it is beneficial to directly and independently test specific parameters and their influence on rainfall. Changing the vegetation type altogether results in changing multiple surface parameters at once (e.g., roughness length, albedo, root zone depth, leaf area index, etc.), and the resulting changes to clouds and rainfall patterns may then be attributable to the effects of multiple parameters as well as their interactions. This makes it difficult to assess the actual processes at work and the individual roles of the different land surface properties.

In order to understand how aerosols, clouds, and surface processes may interact synergistically, the factor separation methodology of Stein and Alpert [1993] was utilized for this analysis. Factor separation is a simple and elegant way to show how multiple factors, as well as their nonlinear interactions, influence a predicted field. The impact of the factors and their interactions is determined through linear combinations. If each factor has two options (e.g., “on” or “off”),  $2^n$  simulations are required if  $n$  factors are investigated. For example, if the influence of two factors, such as topography and surface fluxes, on a particular field, such as total accumulated precipitation, is investigated, then four simulations are required [Stein and Alpert, 1993]. The separate influences of topography and surface fluxes, and the influence of the joint or synergistic interaction between topography and surface fluxes, are determined through linear combinations of the simulations (for example, see the formulae in Table 2). It should be noted that the interpretation of the results obtained from the factor separation calculations, particularly for a field that has a finite range like total

**Table 2.** Experiment Numbering, Nomenclature, and Factor Separation Formulae<sup>a</sup>

Simulation No. (Factor Name)	Experiment Name	Factor Separation Formula	Description
1 (f0)	CTL	-	Base simulation (most pristine)
2 (f1a)	cMid	f1a - f0	Impact of moderate aerosol perturbation
3 (f1b)	cPoll	f1b - f0	Impact of extreme aerosol perturbation
4 (f2a)	tMid	f2a - f0	Impact of moderate roughness length perturbation
5 (f2b)	tSml	f2b - f0	Impact of extreme roughness length perturbation
6 (f3a)	s50	f3a - f0	Impact of moderate soil moisture perturbation
7 (f3b)	s25	f3b - f0	Impact of extreme soil moisture perturbation
8 (f1a2a)	cMid-tMid	f1a2a - (f1a + f2a) + f0	Double synergy between aerosols and roughness length for moderate perturbations
11 (f1b2b)	cPoll-tSml	f1b2b - (f1b + f2b) + f0	Double synergy between aerosols and roughness length for extreme perturbations
12 (f1a3a)	cMid-s50	f1a3a - (f1a + f3a) + f0	Double synergy between aerosols and soil moisture for moderate perturbations
15 (f1b3b)	cPoll-s25	f1b3b - (f1b + f3b) + f0	Double synergy between aerosols and soil moisture for extreme perturbations
16 (f2a3a)	tMid-s50	f2a3a - (f2a + f3a) + f0	Double synergy between roughness length and soil moisture for moderate perturbations
19 (f2b3b)	tSml-s25	f2b3b - (f2b + f3b) + f0	Double synergy between roughness length and soil moisture for extreme perturbations
20 (f1a2a3a)	cMid-tMid-s50	f1a2a3a - (f1a2a + f1a3a + f2a3a) + (f1a + f2a + f3a) - f0	Triple synergy between all three factors for moderate perturbations
27 (f1b2b3b)	cPoll-tSml-s25	f1b2b3b - (f1b2b + f1b3b + f2b3b) + (f1b + f2b + f3b) - f0	Triple synergy between all three factors for extreme perturbations

<sup>a</sup>Simulations including a combination of moderate and extreme perturbations (e.g., simulation 9, cMid-tSml) are not displayed for brevity.

precipitation, is not always trivial. This is discussed in detail in section 3.6. Factor separation has been successfully used in many modeling studies of atmospheric processes, such as lee cyclogenesis [Alpert *et al.*, 1996], aerosol impacts on convective precipitation [van den Heever *et al.*, 2006; Seigel *et al.*, 2013], the influence of land-cover change on convective storm development [Gero and Pitman, 2006], and sea breeze structure [Darby *et al.*, 2002].

Each of the three parameters tested (aerosol concentrations, roughness length, and soil moisture) represents one factor that can impact the spatial and temporal convective rainfall patterns. Generally, 2<sup>n</sup> simulations are required to assess how *n* different factors and their nonlinear interactions influence a solution. Since we used three possible initial values for each of three factors, 3<sup>3</sup> = 27 simulations were necessary. The simulation numbers and names, the corresponding factor separation name, and the factor separation formula used to calculate the influence of each factor and the synergistic interactions among factors are summarized in Table 2. The naming convention to be used throughout the rest of this study will be as follows: simulation 1 will always be called “CTL,” and the sensitivity experiments are referenced by the labels “c” (aerosols or potential CCM), “t” (roughness length or tree height), and “s” (soil moisture), followed by the perturbation description. If a particular label is not included, this means that the value for that factor is the same as in CTL. For example, “cMid-tSml-s25” refers to the simulation with the moderate aerosol perturbation and the most extreme roughness length and soil moisture perturbations, while “cPoll-s50” refers to the simulation with the most polluted aerosol concentrations and the 50% saturated soil moisture perturbation, but with the original, largest value of roughness length as in CTL.

### 3. Results

#### 3.1. CTL Sea Breeze and Precipitation Characteristics

Many of the following figures are presented as subsets relative to the location of the sea breeze front. In order to identify the sea breeze front location at each model output time (every 5 min), the zonal wind was first averaged meridionally and over the lowest 1 km agl, and

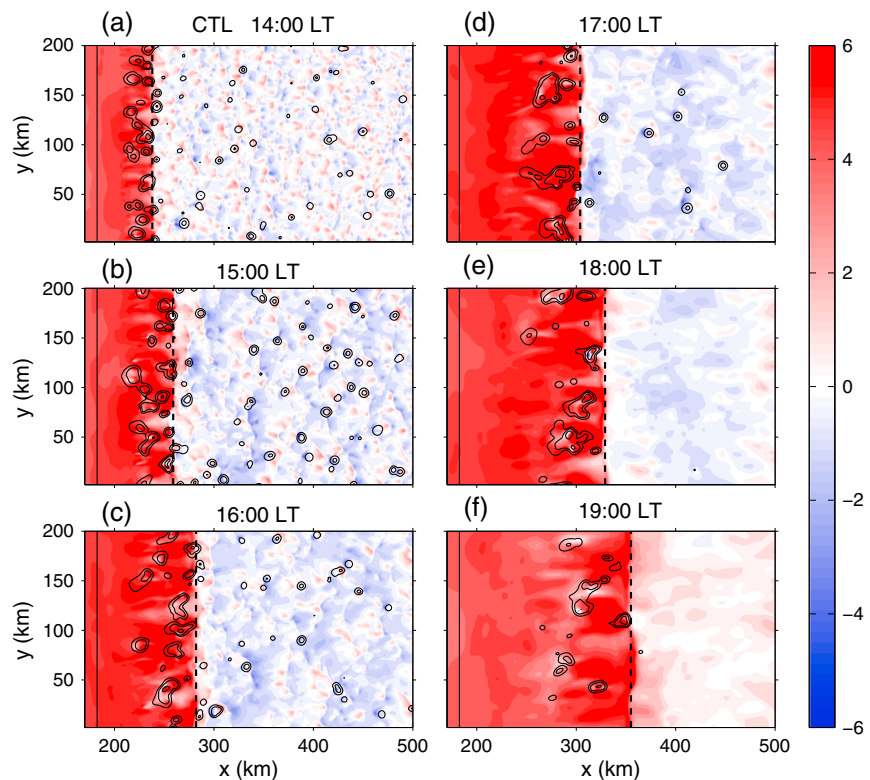


**Figure 3.** Zonal wind vertically averaged over the lowest 1 km ( $\text{m s}^{-1}$ , shaded) and precipitation rate (0.5, 5, and  $50 \text{ mm h}^{-1}$ , solid contours) for simulation CTL, from (a–f) 1400–1900 LT as indicated in each panel. The thin solid line at  $\sim x = 180 \text{ km}$  denotes the ocean-forest border. The thick dashed black line is the identified sea breeze from the averaged convergence as described in the text.

then smoothed to obtain an average zonal wind profile in the east–west direction. The sea breeze location was then identified as the minimum in the gradient of this averaged and smoothed wind profile. This point, which corresponds to the  $x$  location of the maximum averaged zonal wind convergence, was simply extrapolated to all points in  $y$  for simplicity, representing the sea breeze front as a straight line.

Figure 3 displays the vertically averaged 0–1 km zonal wind, the identified sea breeze location, and precipitation rate each hour from 1400 to 1900 LT for CTL. At 1400 LT (Figure 3a), the sea breeze front is well defined by virtue of the differential heating of the land surface that has occurred throughout the morning hours. The sea breeze then propagates eastward and serves as a focal point for convection through convergence at its leading edge. The precipitation rates associated with the sea breeze are increasing at 1400 LT and maximize between  $\sim 1700$  and 1800 LT (Figures 3d and 3e). Most of the sea breeze precipitation dissipates by 2200 LT, 1 h before the end of the simulation. It can be seen in Figure 3 that both the linear sea breeze front approximation and the sea breeze front identification based on the average low-level zonal wind convergence are reasonable. The sea breeze front does vary spatially, especially as it interacts with gust fronts produced by storms ahead of the sea breeze, but this variation is usually not by more than 5–10 km.

In order to further demonstrate the structure of the sea breeze and how it changes in some of the sensitivity experiments, the sea breeze strength expressed in terms of its density potential temperature perturbation [Emanuel, 1994], the cold pools associated with smaller convective cells ahead of the sea breeze, and vertically integrated condensate for simulations CTL, cPoll, s25, and cPoll-s25 are depicted in Figure 4 at 1630 LT, shortly before the most intense sea breeze precipitation occurs. The more intense convection associated with the sea breeze front occurs as the sea breeze collides with cold pools. An example can be seen in CTL (Figure 4a) at  $\sim x = 280, y = 20$ , where the interaction between a cold pool and the sea breeze front has caused the integrated condensate to exceed 25 mm. The precipitation associated with this convective development exceeds  $50 \text{ mm h}^{-1}$  30 min later at 1700 LT (Figure 3d, at the same grid coordinates). It is apparent from the example

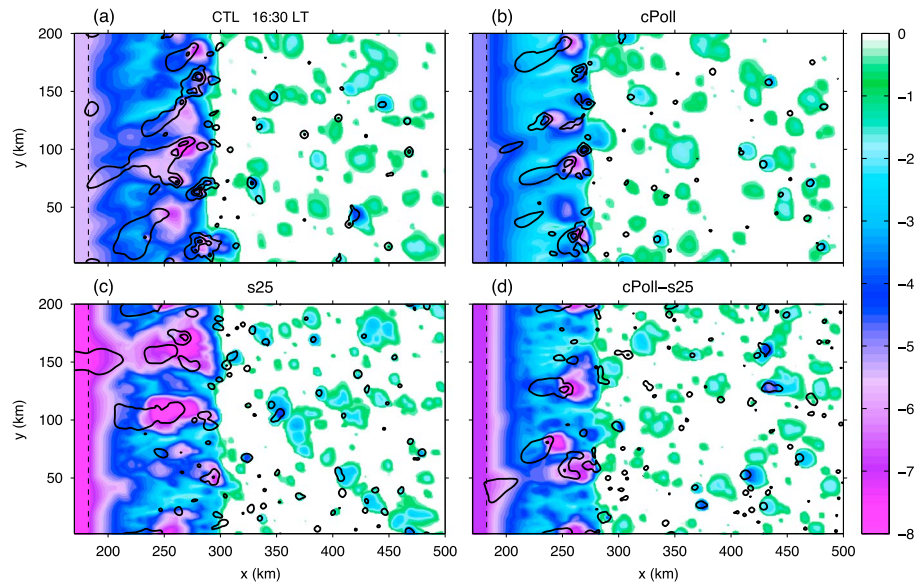


**Figure 4.** Perturbation density potential temperature (K, shaded) at the lowest model level within identified cold pools where buoyancy  $< -0.005 \text{ m s}^{-2}$ , following the methodology of *Tompkins* [2001] and vertically integrated condensate (0.5, 10, and 25 mm solid contours) for simulations (a) CTL, (b) cPoll, (c) s25, and (d) cPoll-s25 at 1630 LT. The mean density potential temperature is determined by spatially averaging the density potential temperature from 10 km ahead of the sea breeze front to 50 km from the east border of the domain. The thin dashed line denotes the forest-ocean border.

shown in Figure 4 that both independent and simultaneous changes to aerosol concentrations and soil moisture impact the sea breeze strength, structure, and propagation, as well as the cloud field and cold pools in the eastern portion of the domain. These changes will be discussed in further detail in the following sections.

Given the idealized nature of the simulations, the intent is not to reproduce the rainfall patterns for a specific event over the Cameroon rainforest. However, it is helpful to know whether the model produces reasonable rainfall totals for this region at this time of year. The precipitation rate in CTL averaged spatially over the forest region and temporally between 1300 and 2200 LT is  $\sim 0.34 \text{ mm h}^{-1}$ . The average precipitation rate over 24 h would then be  $\sim 0.13 \text{ mm h}^{-1}$ . This represents a lower limit approximation for the simulated average precipitation rates, since it assumes that all the precipitation occurs in the afternoon in association with the sea breeze forcing. For comparison, the 24 h accumulated precipitation between the 6 h and 30 h YOTC forecasts initialized at 12 UTC was calculated for each day in June, July, and August in 2008 and 2009 and then temporally averaged (Figure 1b). The ECMWF YOTC average precipitation rate varies between  $\sim 0.2$  and  $0.4 \text{ mm h}^{-1}$  along the Cameroon rainforest coast between  $1^\circ\text{N}$  and  $4^\circ\text{N}$ , which compares well with the  $0.13 \text{ mm h}^{-1}$  lower bound in CTL. Additionally, the RAMS and YOTC precipitation rates agree favorably with estimates of annual mean precipitation from observations for this region between  $1.6$  and  $2.2 \text{ m yr}^{-1}$ , or  $0.18$  to  $0.25 \text{ mm h}^{-1}$  [*Liebmann et al.*, 2012, Figures 1 and 2]. Therefore, the accumulated precipitation associated with the sea breeze convection in the idealized RAMS simulations appears reasonable. The changes to the sea breeze precipitation in each sensitivity experiment are discussed in the next section. The processes by which aerosol concentrations, roughness length, soil moisture, and their sets of nonlinear interactions influence the precipitation amounts and patterns are then investigated by analyzing their impacts on the three ingredients for convection: moisture, instability, and lift.

### 3.2. Sensitivity Experiments: Changes in Precipitation

Figure 5 displays the average accumulated precipitation at the end of the simulation (2300 LT) for (a) all 27 simulations and (b) the results of the factor separation calculation. The naming convention of each simulation and the formulae used to calculate the values in Figure 5b are as described in Table 2. Note that the simulations are color coded according to whether they include only one factor (blue: aerosols, green: roughness length, red: soil moisture), different pairs of factors (pink: aerosols and roughness length, purple: aerosols and soil moisture, orange: roughness length and soil moisture), or all three factors (gold). The same colors are used throughout the rest of the figures in this paper for clarity.

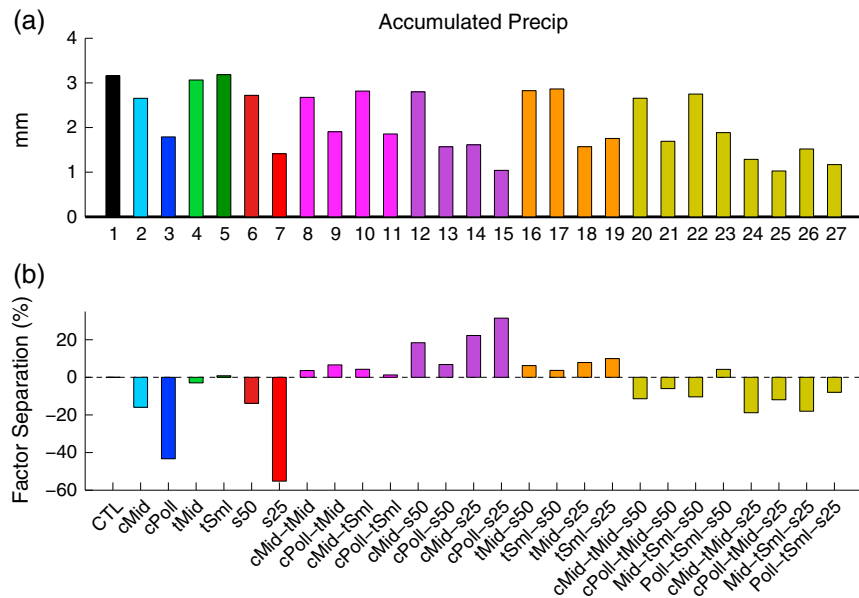


**Figure 5.** (a) Averaged accumulated surface precipitation (mm) over the forest region at the end of the simulation for all 27 experiments. (b) Results of the factor separation calculation (Table 2), expressed as a percentage of CTL. The values displayed for simulations 8–27 are not simply percent differences from CTL, as described in the text. Factor separation for simulations 8–19 represents double synergistic interactions between pairs of factors, and the triple synergistic interactions are represented in simulations 20–27.

The highest accumulated precipitation occurs in simulation 5 (tSml), followed closely by CTL. It is immediately obvious that enhanced aerosol concentrations and reduced soil moisture both individually reduce precipitation totals, by over 40% and 50% for the most extreme perturbations (Figure 5b). The trends in precipitation due to reduced roughness length are nonmonotonic, but the changes in precipitation are quite small. The lowest accumulated precipitation occurs in simulation 25 (cPoll-tMid-s25) where precipitation is reduced from CTL by almost 70%.

By including the simulations containing the combinations of factors (simulations 8–27), the synergistic interactions occurring between the factors can be assessed. It is important to note that these synergy terms, as calculated with the factor separation formulae (Table 2) and displayed in Figure 5b, represent the nonlinear interactions, or feedbacks, acting between the different factors. For example, the synergy between aerosols and soil moisture can either enhance or reduce the rainfall *relative* to the change in rainfall that would occur if the *separate individual* impacts of aerosols and soil moisture were added together. The results of the factor separation calculation displayed in Figure 5b indicate that all the double synergistic interactions between pairs of factors (simulations 8–19) work to enhance accumulated precipitation, while almost all the triple synergistic interactions (simulations 20–27) reduce the precipitation. The interpretation of these signs is not trivial and is discussed in further detail in section 3.6. Note that the double synergy terms are largest for aerosol-soil moisture interactions (simulations 12–15) and that the magnitudes of the double synergy terms for aerosol-roughness length interactions (simulations 8–11) are all larger than the impacts of roughness length itself (simulations 4–5).

The separate impacts of (1) increased aerosol concentrations, (2) reduced surface roughness length, (3) reduced soil moisture, and then the synergistic interactions among these three factors on the precipitation fields, as well as a discussion of the processes responsible for the precipitation trends noted above, are presented in the following four sections.

### 3.3. Enhanced Aerosol Concentrations

The focus of this section is on the reduction in accumulated precipitation that occurs in simulations cMid and cPoll relative to CTL (Figure 5). Ammonium sulfate aerosols scatter and absorb radiation depending on the wavelength, the aerosol median size, and the relative humidity [Saleeby and van den Heever, 2013]. Thus,

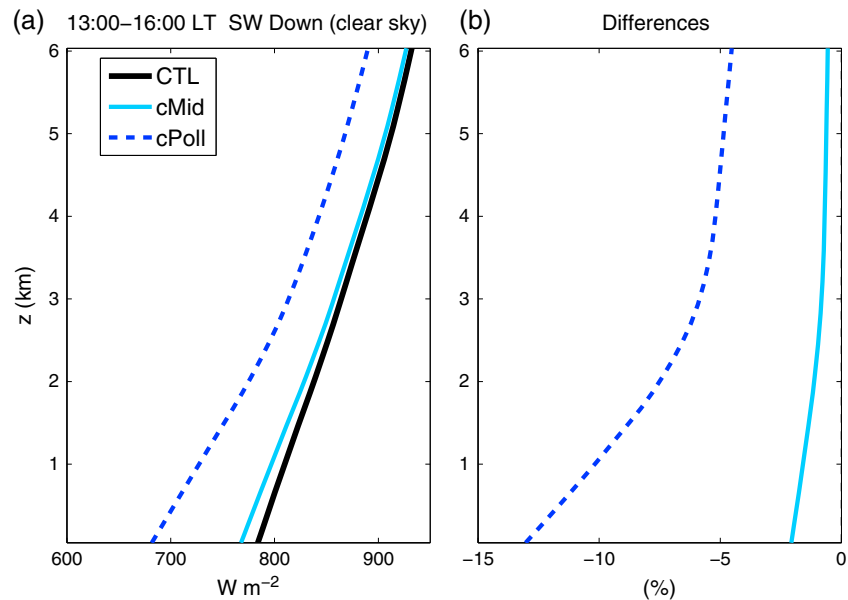


**Figure 6.** (a) Downwelling shortwave radiation ( $\text{W m}^{-2}$ ) and (b) percent change from CTL for simulations CTL, cMid, and cPoll, averaged from 1300 to 1600 LT and from 10 km ahead of the sea breeze front (in order to avoid any spatial variation in the sea breeze front location) to 50 km from the eastern domain edge for clear-sky columns only. Clear-sky columns required that total condensate  $< 0.01 \text{ g kg}^{-1}$  everywhere throughout the column.

when aerosol concentrations are enhanced, the amount of incoming solar radiation is reduced due to aerosol direct effects. Figure 6 displays profiles of downwelling clear-sky solar radiation averaged ahead of the sea breeze from 1300 to 1600 LT, when incoming solar radiation is near its peak. It is clear that the incoming solar radiation is decreased throughout the atmosphere in cMid and cPoll relative to CTL, especially below  $\sim 3 \text{ km}$  where the aerosol perturbation is concentrated. The downwelling shortwave at the surface is reduced by  $16 \text{ W m}^{-2}$  (2.1%) and  $102 \text{ W m}^{-2}$  (13%) in cMid and cPoll, respectively. These magnitudes are comparable with previous studies investigating aerosol direct effects [Yu *et al.*, 2002; Feingold *et al.*, 2005; Barbaro *et al.*, 2014] (the optical depth in the visible band for simulation cPoll is  $\sim 0.72$ ).

Reductions to the incoming shortwave radiation result in lower surface temperatures in the polluted scenarios. Since the temperature difference between land and ocean is the fundamental driver of the sea breeze, the sea breeze itself weakens, as demonstrated in Hovmöller diagrams of the meridionally and 0–1 km agl vertically averaged zonal wind speed in CTL and the differences between cMid or cPoll and CTL (Figure 7). Wind speeds both behind the sea breeze front and ahead of the sea breeze are weaker in cMid and cPoll. The sea breeze front is also displaced farther west, by  $\sim 40 \text{ km}$  in cPoll at 2200 LT (Figure 7c). The weaker wind speeds and more slowly progressing sea breeze decrease the mean sea breeze convergence by  $\sim 4\%$  and  $14\%$  in cMid and cPoll, respectively (Figure 9). As the convection is driven by the sea breeze, and most of the intense convection is focused just behind the sea breeze front (Figure 3), the accumulated precipitation is lower in cMid and cPoll than in CTL.

Evapotranspiration from the vegetation canopy and the soil is also reduced due to the change in incoming shortwave radiation under enhanced aerosol concentrations. Surface latent heat fluxes (LHFs) and sensible heat fluxes (SHFs) are reduced by  $\sim 4\%$  and  $\sim 6\%$  in cMid and by  $21\%$  and  $\sim 26\%$  in cPoll, respectively (Table 3), which results in less convective available potential energy (CAPE) available to the convection in the afternoon and early evening hours. (This fact is not necessarily reflected in the temporal mean of CAPE that is tabulated in Table 3, as discussed further in section 3.6 and shown in Figure 14a). The Bowen ratio (SHF/LHF), which represents the surface energy flux partition, is slightly smaller under more polluted conditions, since the reduction in SHF is greater than the reduction in LHF. Such aerosol-radiative interactions and subsequent reductions in the surface fluxes, with resultant implications for cloud formation, have also been noted in previous observational and modeling studies [Yu *et al.*, 2002; Koren *et al.*, 2004, 2008; Feingold *et al.*, 2005; Jiang and Feingold, 2006; Zhang *et al.*, 2008].

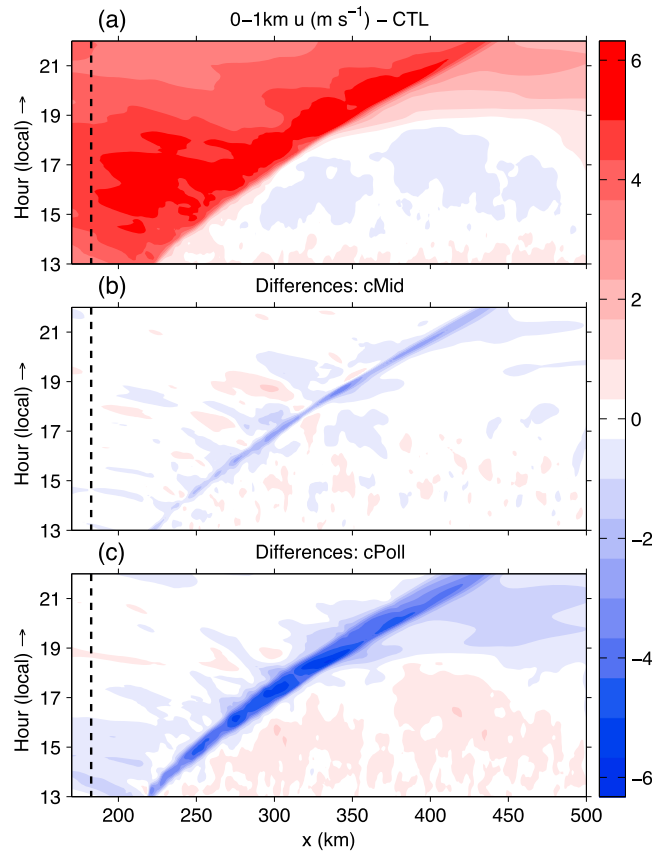


**Figure 7.** (a) Hovmöller diagram of zonal wind ( $\text{m s}^{-1}$ , shaded) averaged meridionally and over the lowest 1 km for simulation CTL, and difference fields for the zonal wind Hovmöller diagrams between simulations (b) cMid and CTL and (c) cPoll and CTL. The dashed black line denotes the forest-ocean border.

Many recent studies investigating aerosol indirect effects on deep convection have found evidence of convective invigoration, whereby elevated aerosol concentrations lead to suppressed warm rain formation, more supercooled liquid water within the mixed phase region, and enhanced latent heating through freezing, which invigorates the convective updrafts and hence can increase precipitation [e.g., *Andreae et al., 2004; Khain et al., 2005; van den Heever et al., 2006*]. Average profiles of vertical velocity exceeding  $1 \text{ m s}^{-1}$  for CTL, cMid, and cPoll indicate that updraft speeds are enhanced by up to 10% within the mixed phase region with increasing aerosol loading, thus demonstrating evidence of weak aerosol-induced convective invigoration in these simulations. It is interesting to note that, in spite of the aerosol-induced invigoration, precipitation is reduced. Therefore, the aerosol direct effects on the surface fluxes and sea breeze strength appear to overwhelm any aerosol indirect effects on the updraft strength and precipitation intensity. In summary, all three ingredients for convection—moisture from evapotranspiration, instability achieved through surface

heating, and sea breeze convergence forcing for ascent—are weakened under scenarios of enhanced aerosol concentrations, explaining the reductions in accumulated precipitation (Figure 5).

### 3.4. Reduced Surface Roughness Length

In this section, changes to the ingredients for convection with decreasing roughness length in simulations 1, 4, and 5 (CTL, tMid, and tSml) are investigated in order to understand why the roughness length does not have a large impact on the sea breeze precipitation (Figure 5). Cross sections of meridionally and temporally averaged zonal wind speeds relative to the sea breeze front in CTL (Figure 8a), and differences between the roughness length sensitivity experiments and CTL (Figures 8b and 8c), demonstrate changes to the structure of the sea breeze in simulations tMid and tSml. A smaller value of surface roughness length results in reduced

**Table 3.** Latent (LHF) and Sensible (SHF) Heat Fluxes, Mixed Layer CAPE, and the Bowen Ratio<sup>a</sup>

Simulation Name	LHF ( $\text{W m}^{-2}$ )	SHF ( $\text{W m}^{-2}$ )	ML-CAPE ( $\text{J kg}^{-1}$ )	Bowen Ratio (SHF/LHF)
CTL	257.4	91.6	1513	0.36
cMid	246.6 (−4.2%)	86.5 (−5.6%)	1519 (+0.4%)	0.35 (−1.5%)
cPoll	203.3 (−21.0%)	67.7 (−26.1%)	1462 (−3.4%)	0.33 (−6.5%)
tMid	248.4 (−3.5%)	98.5 (+7.5%)	1472 (−2.7%)	0.40 (+11.3%)
tSml	229.2 (−10.9%)	105.8 (+15.4%)	1391 (−8.1%)	0.46 (+29.6%)
s50	203.5 (−20.9%)	106.6 (+16.7%)	1334 (−11.9%)	0.53 (+47.7%)
s25	46.1 (−82.1%)	218.9 (+139.0%)	730 (−51.8%)	4.75 (+1235%)

<sup>a</sup>The LHF, SHF, and mixed layer CAPE are averaged spatially from 10 km ahead of the sea breeze to 50 km from the domain edge and temporally from 1300 to 2200 LT. Percent differences from CTL are listed in parentheses in all columns.

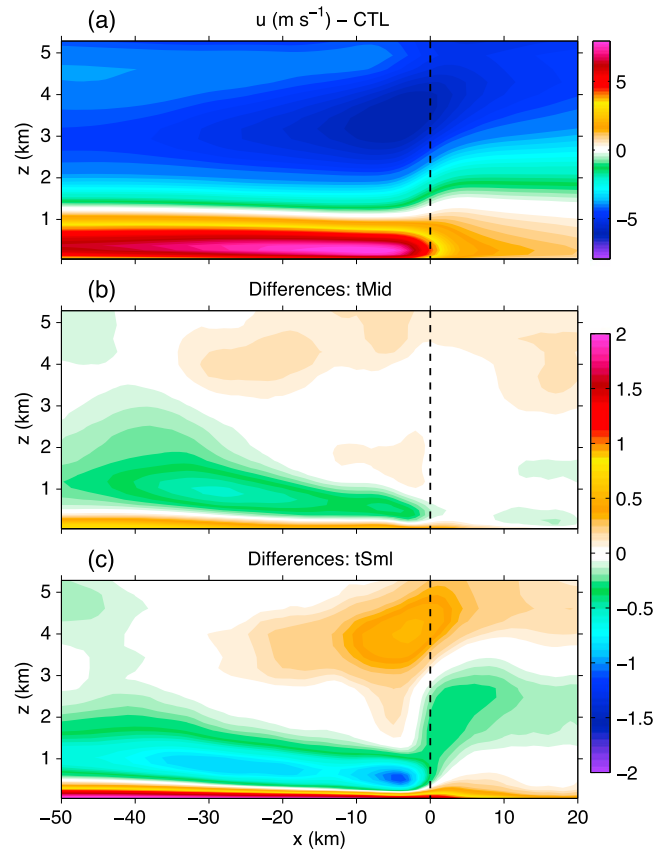


**Figure 8.** (a) Composite cross section of zonal wind speed ( $\text{m s}^{-1}$ , shaded) relative to the sea breeze front (at  $x = 0$ ), averaged meridionally and from 1300 to 2200 LT for simulation CTL, and difference fields for the composite zonal wind cross sections between simulations (b) tMid and CTL and (c) tSml and CTL.

friction velocity and weaker momentum transfer between the surface and lower atmosphere. The net result of these effects is that near-surface zonal wind speeds are stronger, particularly behind the sea breeze but also out ahead of the sea breeze front (Figures 8b and 8c).

The changes in near-surface wind speeds in and around the sea breeze front impact the mean profile of convergence (Figure 9). The peak convergence associated with the sea breeze front is closer to the surface by up to several hundred meters in the smaller surface roughness cases. Convergence at the surface is also enhanced by  $\sim 17\%$  and  $\sim 47\%$  in tMid and tSml. Gero and Pitman [2006] have also demonstrated sensitivity of the sea breeze convergence and resulting convection over the Sydney Basin to changes in the roughness length. Enhanced convergence closer to the surface is more favorable for convection, since the lift associated with the convergence will supply higher moisture and energy from closer to the surface to the developing convection. On the other hand, a lowering of the level of maximum convergence, in conjunction with increases in the lifting condensation level (LCL) and level of

free convection (LFC) associated with a larger Bowen ratio as discussed next, may also result in fewer parcels reaching their LCLs and LFCs.

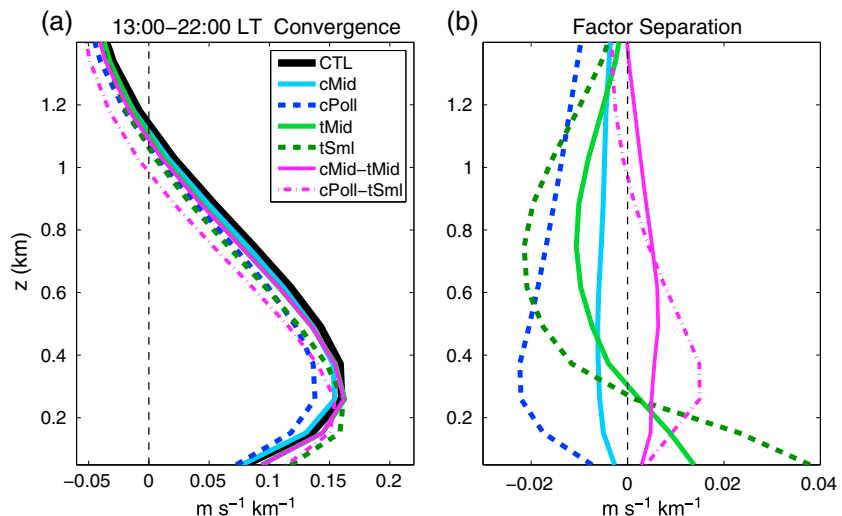


**Figure 9.** (a) Profiles of convergence ( $\text{m s}^{-1} \text{ km}^{-1}$ ) and (b) factor separation calculations for simulations CTL, cMid, cPoll, tMid, tSml, cMid-tMid, and cPoll-tSml, averaged from 20 km behind to 20 km ahead of the sea breeze front and from 1300 to 2200 LT.

The partitioning between the surface SHF and LHF also changes with changing roughness length. The SHF increases by up to ~15% while LHF decreases by up to ~11% as roughness length decreases, which increases the Bowen ratio (Table 3), in agreement with previous studies [Garratt, 1993]. The change in the Bowen ratio with decreasing roughness length occurs because the efficiency of turbulent energy transfer from the canopy to the lower atmosphere decreases, which allows larger surface temperatures to build up and consequently the SHF to increase. While the stronger SHF strengthens surface-driven buoyancy and warms the near-surface air, thereby steepening low-level lapse rates, the smaller LHF reduces the amount of moisture available to the convection. The net result of these two effects is a reduction in the CAPE ahead of the sea breeze (Table 3).

In these experiments, the roughness length was modified without changing any of the other land surface parameters. In reality, it is likely that other surface parameters, such as leaf area index (LAI) and rooting depth, are also altered when the roughness length is decreased, although often all three of these surface parameters increase toward their original values with forest regrowth [Mahmood *et al.*, 2014]. The duration of these idealized simulations is not long enough for precipitation and evaporation to change the soil moisture below a depth of 0.3 m. Therefore, the results presented herein are not expected to be sensitive to the root zone depth, since the smallest root depth for any vegetation type in LEAF is 0.7 m. In order to test the sensitivity to both LAI and roughness length, additional simulations were performed in which LAI was varied between ~0.5 and 6 for the smallest roughness length case, where 6 is the maximum value of LAI for the LEAF evergreen broadleaf vegetation class. It was found that LAI also has a nonmonotonic impact on the precipitation. The largest change in the magnitude of accumulated precipitation with changing LAI was ~7% relative to simulation tSml. The impacts of LAI are similar to those of roughness length in that a smaller LAI increases the Bowen ratio, which increases the strength of the sea breeze convergence but decreases the CAPE. These have competing effects on the convection. The sea breeze precipitation is therefore not very sensitive to changes in LAI associated with different roughness lengths, especially in comparison to the precipitation sensitivity to aerosols and soil moisture (Figure 5).

In summary, the three ingredients for convection change in compensating ways when surface roughness length is decreased. While the strength of the convergence increases and its peak is closer to the surface, the low-level moisture and therefore CAPE both decrease. These competing effects on convection produce only small changes to the total rainfall.

### 3.5. Reduced Soil Moisture

The differences in rainfall between simulations 1, 6, and 7 (CTL, s50, and s25) are discussed in this section. It was seen in section 3.2 that the accumulated rainfall is substantially reduced as soil moisture content is decreased to 25% saturation. It is also clear from Figure 5 that the precipitation responds nonlinearly to a linear decrease in soil moisture content. The sea breeze structure response to the soil moisture perturbation is also highly nonlinear, as evidenced in Hovmöller plots of the zonal wind speed (Figure 10). The wind speeds behind the sea breeze are stronger and the sea breeze front is 15 km farther eastward at 2200 LT in simulation s25 compared to CTL (Figure 10c), in agreement with previous studies demonstrating changes to the sea breeze propagation speed with varying soil moisture [Physick, 1980; Miao *et al.*, 2003]. Due to these changes in the zonal wind speed, the sea breeze convergence is significantly enhanced, by up to 100% at ~1 km agl in s25 (not shown), although it is only very slightly enhanced in s50 relative to CTL.

The sea breeze is stronger in s25 because the LHF is reduced while the SHF is enhanced, and hence, the Bowen ratio is increased, under drier soil conditions (Table 3), in agreement with previous studies [Physick, 1980; Kala *et al.*, 2010]. Again it is apparent that the increase (decrease) in SHF (LHF) responds highly nonlinearly to the soil moisture perturbation. This nonlinear response is a result of the parameterized vegetation becoming stressed when the soil moisture is reduced to 25% saturation. Since more of the shortwave radiation absorbed at the surface is utilized to increase the surface temperature rather than to flux water to the atmosphere under lower soil moisture scenarios, the forest-ocean temperature gradient increases. The sea breeze strength therefore also increases, and it accelerates inland more quickly. Robinson *et al.* [2013] have also recently demonstrated a similar result within idealized two-dimensional simulations of sea breeze propagation under varying magnitudes of surface heating.

In summary, reduced soil moisture alters the three ingredients for convection in opposing ways. Although the convergence associated with the sea breeze front strengthens, the reduction in the LHF limits the amount of

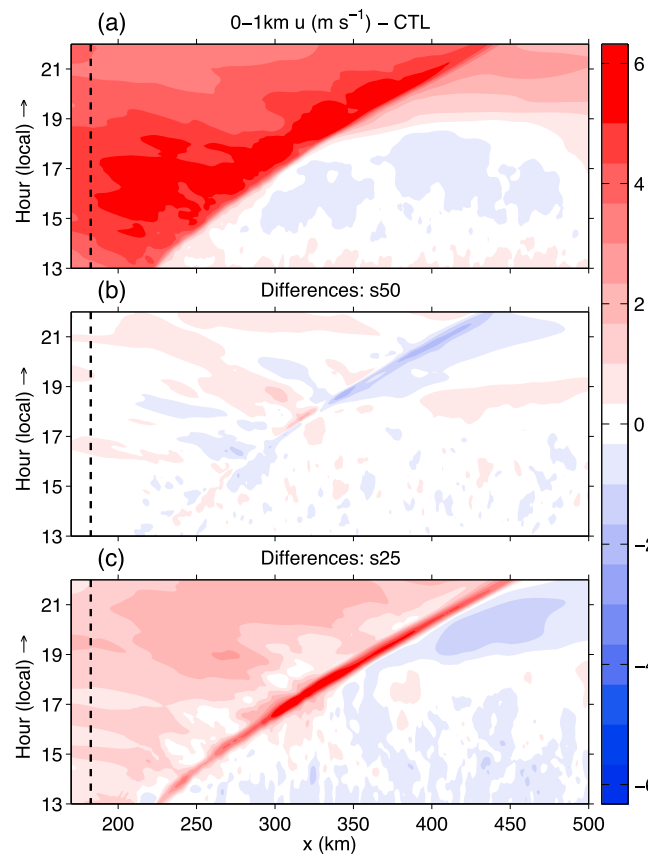


Figure 10. As in Figure 7 but for simulations CTL, s50, and s25.

moisture and therefore CAPE available to the convection (Table 3). Near-surface vapor mixing ratios are reduced by  $0.6 \text{ g kg}^{-1}$  (4%) in s50 and by  $3 \text{ g kg}^{-1}$  (20%) in s25. Therefore, the moisture reduction has the greatest control over the precipitation response in s25. The reductions in low-level moisture and CAPE are also associated with increases in the LCL and LFC, and therefore, fewer parcels are able to be lifted to their LFCs and realize their convective buoyancy. This result is similar to that described by Baker *et al.* [2001]; they showed that precipitation associated with Florida sea breeze convection was higher over wetter soils because low-level moisture and instability were increased. Ramos da Silva and Avissar [2006] also found that wetter soil conditions led to more precipitation in simulations of convection over Amazonia. The impact of reduced soil moisture on the sea breeze precipitation is analogous to the impact of reduced roughness length, wherein convergence is strengthened but an increase in the Bowen ratio results in less available moisture and CAPE.

### 3.6. Synergistic Interactions

In this section, possible feedbacks to rainfall patterns resulting from the nonlinear interactions of aerosols and land surface processes are discussed. Recall that Figure 5b displays the results of the factor separation calculations. It should be emphasized that the double and triple synergy terms are not simply the differences in rainfall between each simulation and CTL but rather represent the contributions of the synergistic interactions that occur only when both effects are present (Table 2). For simulations 8–19, the factor separation calculation therefore represents the impact on the rainfall that is solely due to the interaction, or synergy, between the pairs of factors being considered by subtracting out the individual separate contributions of each factor. In simulations 20–27, the triple interactions between aerosols, roughness length, and soil moisture are demonstrated.

The factor separation results for accumulated precipitation (Figure 5b), calculated using the formulae provided in Table 2, demonstrate that the double synergies all act to enhance total rainfall, while the triple interaction reduces rainfall. However, care must be taken in interpreting the synergy calculation when one of the factors dominates the solution [Alpert and Sholokhman, 2011]. For instance, the accumulated precipitation is reduced by almost 60% when soil moisture is reduced to 25% saturation (Figure 5b). Additionally, for the most polluted aerosol scenario, precipitation is reduced by ~40%. Since the individual impact of each of these factors is large, a negative feedback by synergy between these two effects naturally arises from the calculation (Table 2) because accumulated rainfall is a finite quantity that cannot be reduced indefinitely. Note that this is also generally true when using factor separation analysis to interpret changes in any quantity that has a finite range. In these scenarios, the synergy terms are not as meaningful because the individual impacts of soil moisture and aerosols dominate the rainfall changes.

On the other hand, feedbacks and more meaningful synergy contributions emerge when perturbations are moderate or the rainfall response to the individual factor is small. For instance, the synergy between

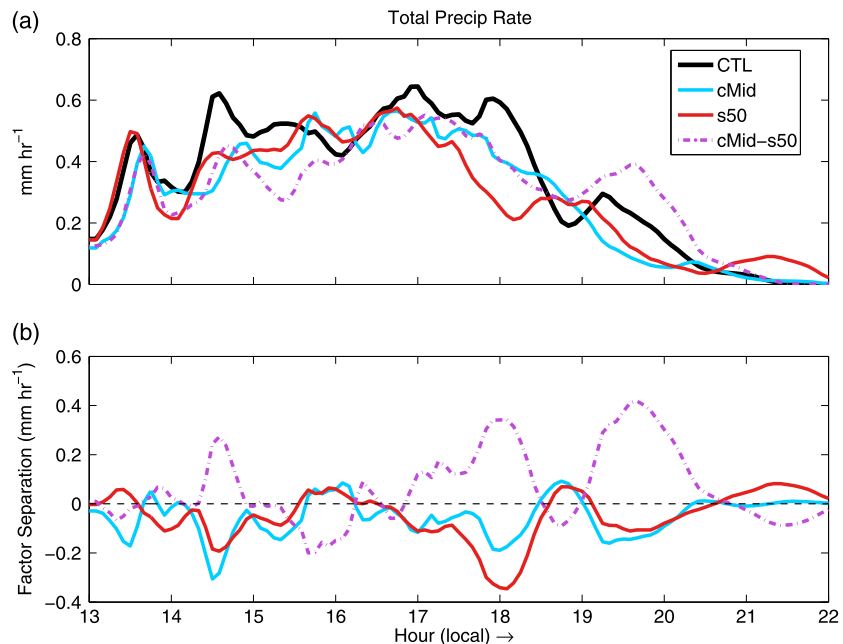


**Figure 11.** (a) Time series of the rate of change of accumulated precipitation ( $\text{mm h}^{-1}$ ) averaged over the forest region and (b) the factor separation calculation for simulations CTL, cMid, s50, and cMid-s50. Note that the cMid-s50 line in Figure 11b represents the double synergy term.

roughness length and aerosols always increases rainfall and almost always by more than the individual impact of roughness length itself (Figure 5b). Also, interestingly, while precipitation is reduced in both cMid and s50 relative to CTL as described above, the accumulated precipitation in simulation cMid-s50 is larger than in either cMid or s50 itself, indicating the importance of the synergistic interactions that act to enhance rainfall in this case. The magnitude of the contribution by synergy to the rainfall enhancement is  $\sim 20\%$ , which is larger than the individual magnitudes of the rainfall reduction by cMid and s50. This synergy represents a negative feedback to the rainfall, since it acts in opposition to the individual negative impacts of aerosols and soil moisture. The processes responsible for the rainfall enhancement by synergistic interactions between aerosols and soil moisture for moderate perturbations are next explored to demonstrate how such nonlinear interactions arise.

A time series of the rate of change of the accumulated precipitation over the forest region (Figure 11) demonstrates that the enhanced precipitation by cMid-s50 synergy occurs primarily in the latter half of the analysis period. The most significant magnitude and percentage increase in precipitation rate occurs between 1900 and 2100 LT as the sea breeze convection diminishes. In simulation cMid-s50, individual convective towers develop ahead of the sea breeze between 1800 and 1830 LT. Their respective outflows at 1905 LT, which are characterized by strong divergence at the centers and convergence along their edges, are evident in Figure 12d at  $\sim x = 350, y = 80$  km. These outflows interact with the sea breeze front, locally enhancing convergence and further increasing convection behind the sea breeze from 1900 to 2000 LT. Additionally, convergence is enhanced directly to the north and south of where the outflows intersect the sea breeze front. Vertically integrated condensate begins to increase there, similarly to the mechanism described in *Droegemeier and Wilhelmson* [1985]. Although convection along the sea breeze still occurs toward the end of the simulations in CTL, cMid, and s50 (such as the convection seen at  $x = 350, y = 120$  in CTL (Figure 12a) after the sea breeze interacts with an older remnant cold pool), strong individual convective towers ahead of the sea breeze are only able to develop in simulation cMid-s50, when *both* enhanced aerosol concentrations and reduced soil moisture are included. The presence of this convection and the subsequent enhancement of the sea breeze precipitation resulting from its outflow therefore demonstrate how the nonlinear interactions between aerosols and soil moisture operate. This mechanism is consistent with the findings in *Baker et al.* [2001]. They indicated that nonlinear interactions between coastline curvature and land breeze circulations increase precipitation due to local enhancements in sea breeze convergence resulting from gust fronts.

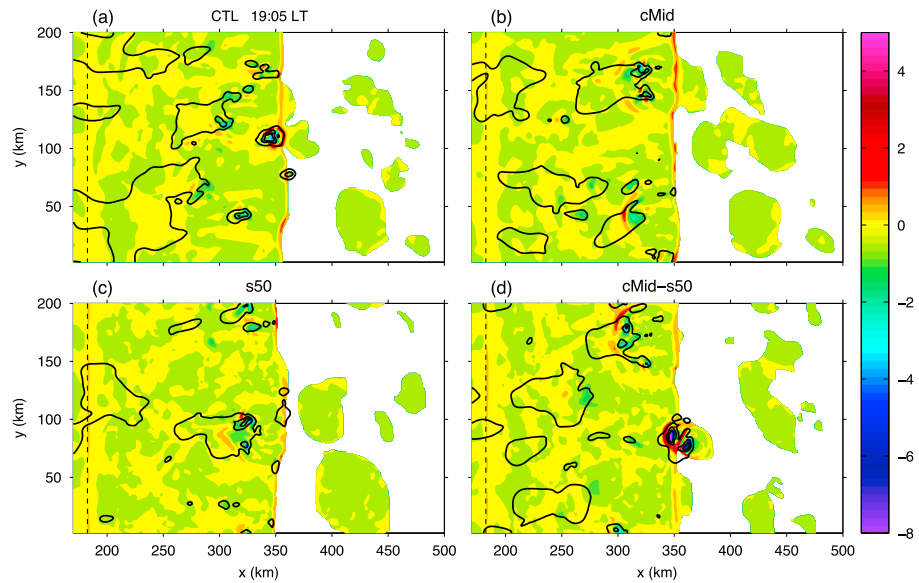


**Figure 12.** Convergence at the lowest model level ( $\text{m s}^{-1} \text{ km}^{-1}$ , shaded only within identified cold pools, as in Figure 4) and vertically integrated condensate (0.5, 10, and 25 mm, solid contours) for simulations (a) CTL, (b) cMid, (c) s50, and (d) cMid-s50 at 1905 LT. The thin dashed line denotes the forest-ocean border.

The formation of the convection ahead of the sea breeze in cMid-s50 can be understood as follows: In more polluted scenarios, there are fewer clouds ahead of the sea breeze, as demonstrated by the average total condensate profile shown in Figure 13. This occurs due to the reduced surface fluxes as well as smaller cloud

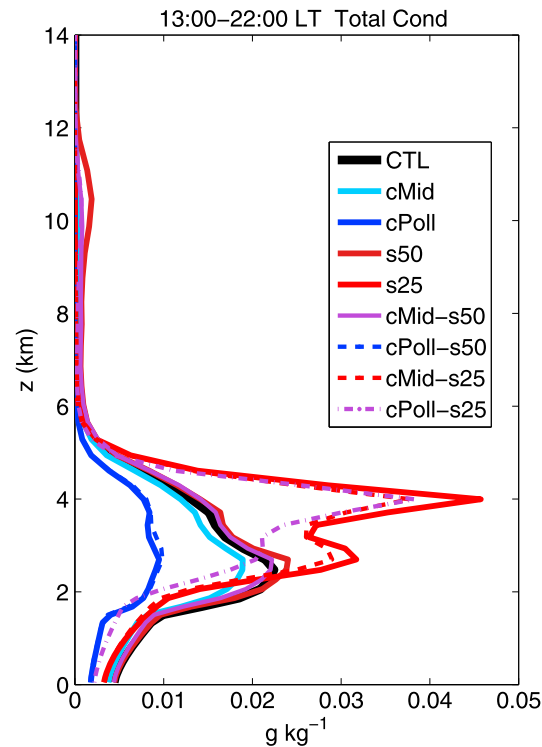


**Figure 13.** Profiles of total condensate ( $\text{g kg}^{-1}$ ) averaged spatially from 10 km ahead of the sea breeze front to 50 km from the eastern domain edge, and temporally from 1300 to 2200 LT, for all aerosol and soil moisture experiments.

droplets and hence enhanced evaporation rates with increased aerosol concentrations (not shown). Similar results have been found in previous studies [e.g., Koren *et al.*, 2004; Feingold *et al.*, 2005; Jiang and Feingold, 2006; Xue and Feingold, 2006]. Thus, although the surface fluxes are reduced with enhanced aerosol concentrations (Table 3), the evening CAPE (after 1900 LT) ahead of the sea breeze is larger in cMid because less convection has utilized and hence erased the instability in this region (Figure 14a). When soil moisture is reduced and the Bowen ratio increases, the surface buoyancy forcing increases and moisture decreases. This results in enhanced cloudiness above  $\sim 3$  km (Figure 13) and fewer clouds that develop into deep convection under drier soil conditions. Additionally, cold pools ahead of the sea breeze are stronger on average by 0.11 K ( $\sim 13\%$ ) in s50 and by 0.14 K ( $\sim 17\%$ ) in s25 relative to CTL in terms of their density potential temperature perturbations, which is evident qualitatively in Figure 4. It is only when both of these effects are present (larger evening instability with enhanced aerosols and stronger surface buoyancy fluxes and forcing by cold pool outflows with reduced soil moisture) that evening convection ahead of the sea breeze is able to develop and subsequently interact with the sea breeze to locally enhance the precipitation.

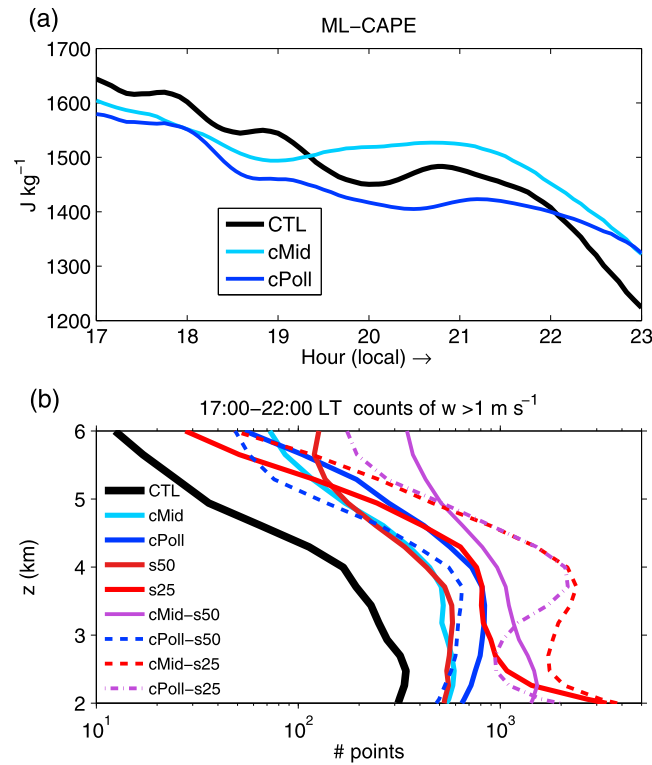


**Figure 14.** (a) Time series of mixed layer CAPE averaged spatially from 10 km to 75 km ahead of the sea breeze for CTL and the enhanced aerosol experiments. (b) Profiles of the number of grid points with vertical velocity exceeding  $1 \text{ m s}^{-1}$  ahead of the sea breeze (10 km from the sea breeze front to 50 km from the eastern domain edge) from 1700 to 2200 LT for all aerosol and soil moisture experiments.

Although the specific mechanism of cold pool formation and interaction with the sea breeze front has been demonstrated in only one simulation, cMid-s50, at one time, the same sequence of events also occurs at earlier times in cMid-s50, which is evident in the precipitation rates between 1700 and 1800 LT (Figure 11), as well as in the other simulations incorporating combinations of aerosols and surface fluxes. This result is evident in the counts of vertical velocity exceeding  $1 \text{ m s}^{-1}$  ahead of the sea breeze (Figure 14b). The vertical velocity counts are taken between 1700 and 2200 LT, the time period during which precipitation is enhanced by aerosol-soil moisture synergy, and between 2 and 6 km agl, the range of heights to which cold pool-producing convection ahead of the sea breeze rises. Except for simulation cPoll-s50, there are substantially more counts of vertical velocity in the simulations containing both aerosols and surface fluxes than in CTL and the simulations with only aerosol or soil moisture perturbations (note the log scale for the x axis in Figure 14b).

Finally, the nonlinear interactions between aerosols and roughness length are analogous to those between aerosols and soil moisture because, as in the simulations with reduced soil moisture, reductions in roughness length also result in a larger Bowen ratio and stronger convective outflows. Factor separation calculations demonstrate that synergistic interactions between aerosols and roughness length enhance the sea breeze convergence by up to 37% (Figure 9; only cMid-tMid and cPoll-tSml are shown for clarity), which enhances the rainfall.

To summarize, soil moisture and aerosol loading individually dominate the impacts on rainfall when the perturbations are extreme, but the nonlinear interactions between aerosols and soil moisture and between aerosols and roughness length are significant when aerosol and soil moisture perturbations are more moderate. These interactions arise through their synergistic impacts on the third ingredient for convection, the lifting mechanism. This result demonstrates the chaotic nature of convection, as has also been noted by Carbone *et al.* [2000] for observations of organized convection initially forced by sea breeze and gust front interactions over the Tiwi Islands and by Baker *et al.* [2001] within Florida sea breeze simulations. The sensitivity of convective rainfall to small changes in the ingredients for convection and hence initial convective forcing in these simulations highlights this chaotic nature, since the enhanced rainfall by synergy depends on the presence or absence of relatively stronger convection that initiates ahead of sea breeze. In turn, the gust fronts locally enhance the sea breeze convergence and therefore the sea breeze precipitation.

#### 4. Summary and Discussion

In this study, the relative influences of aerosols, surface roughness length, and soil moisture, as well as their synergistic interactions, on the rainfall resulting from tropical convection focused along a sea breeze front have been investigated through the use of idealized cloud-resolving modeling simulations. The impacts of these factors and their interactions on the rainfall were investigated by analyzing the three ingredients for

convection: moisture, instability, and lift. It was shown that enhanced aerosol number concentrations reduce the amount of shortwave radiation absorbed at the surface, resulting in less surface heating and smaller surface fluxes, a weaker sea breeze, and therefore reduced rainfall. Reduced soil moisture also reduces rainfall by changing the SHF and LHF partition and therefore the Bowen ratio. The smaller LHF results in less low-level moisture available to the convection and consequently lower precipitation totals. A smaller surface roughness length leads to enhanced convergence along the sea breeze front but reduced moisture and instability through increases in the Bowen ratio. Changes to the roughness length therefore have competing effects on the ingredients for convection, and the net result is that changes to rainfall are small.

This study has also demonstrated that when the perturbations to aerosol concentrations or soil moisture are more extreme, their influences on the surface fluxes and available low-level moisture dominate the resulting changes to the sea breeze rainfall. However, nonlinear interactions between aerosols and land surface processes, particularly between aerosols and soil moisture, are more significant when their relative perturbations are more moderate. These interactions act to enhance rainfall, which represents a negative feedback to the precipitation, through their mutual impact on the sea breeze convergence and storm-generated gust fronts interacting with the sea breeze front. Therefore, these results indicate that the pathway through which such interactions between aerosols and land surface processes can occur is primarily through the low-level convergence.

Given the idealized nature of the simulations, it is possible that these results are also more generally applicable to tropical rainforest convection initiated along other boundaries such as sea breezes in Amazonia and Indonesia, or lake breezes along Lake Victoria, which have been shown to be important forcing mechanisms for deep convection that contribute to the spatial pattern of rainfall over tropical rainforests [Kousky, 1980; Laing *et al.*, 2008, 2011; Vondou *et al.*, 2010]. However, the sensitivity to the initial thermodynamic and wind profile, which is representative of the coastal Cameroon rainforest region in this study, remains to be tested and is an important next step, given the influence that shear and instability have on deep convection and rainfall totals. It will also be important to account for other local factors that may modulate the sensitivities of the sea breeze convection to changing aerosol concentrations and land surface properties, such as topography and coastline curvature [e.g., Baker *et al.*, 2001; Darby *et al.*, 2002; Miao *et al.*, 2003], which have not been investigated in this study. Additionally, the sole use of ammonium sulfate to represent aerosol effects is an obvious simplification. The Cameroon rainforest region is also characterized by other aerosol types, including mineral dust and biomass burning-derived smoke aerosols, as are other tropical rainforest regions. It is possible that a more absorbing aerosol type, such as black carbon, may further enhance the aerosol effects found in this study. Absorbing aerosol can change the atmospheric stability profile, which could suppress convection and rainfall. Furthermore, shortwave radiation absorbed at the surface decreases as single scattering albedo is decreased [Yu *et al.*, 2002; Barbaro *et al.*, 2014]. Therefore, a more absorbing aerosol than ammonium sulfate may further reduce the sea breeze strength and precipitation by reducing the surface fluxes. However, the impact of different aerosol types remains to be tested. Finally, future work should investigate possible precipitation feedbacks and the role of the land breeze and subsequent sea breezes in initiating and contributing to coastal rainfall totals over several days. Such investigations would require longer duration simulations and therefore lateral boundary nudging with reanalysis data.

The results of this study highlight the importance of considering synergistic impacts of aerosols and land surface properties on clouds and precipitation, as their interactions can be significant. To our knowledge, only one other study has investigated aerosol-cloud-land surface interactions within a coupled system. In their simulations of cumulus convection over land, Jiang and Feingold [2006] found that the inclusion of radiative feedbacks to the surface fluxes by aerosols and clouds resulted in a reduction in the magnitude of the second aerosol indirect effect. Their findings therefore also demonstrate the importance of including such feedbacks. The results of the present study also point to the importance of accurately representing gust fronts and low-level convergence in model simulations, since this is an important mechanism through which these feedbacks occur. Finally, this study underscores the need to account for the surface-cloud-atmosphere system responses to changes in aerosol loading and land surface properties in regional and large-scale models, especially as anthropogenic activity continues to impact tropical rainforest regions. Additional avenues for feedbacks between aerosols and surface processes likely also exist. For example, aerosols and clouds impact the diffuse and direct light partition, which influences evapotranspiration and vegetative

carbon uptake [Gu et al., 2003; Lu et al., 2005; Matsui et al., 2008]. The roughness length may also influence surface emissions of aerosols through changes in the near-surface winds [Cowie et al., 2013]. Such feedbacks must be considered in future studies of aerosol-cloud-land surface interactions.

### Acknowledgments

The ECMWF YOTC data used to create Figure 1 and the initial thermodynamic and wind profile for the idealized RAMS simulations are available at [http://apps.ecmwf.int/datasets/data/yotc\\_od/](http://apps.ecmwf.int/datasets/data/yotc_od/). The RAMS simulation data are available upon request from Leah Grant (ldgrant@atmos.colostate.edu). This research has been supported by a Graduate Student Fellowship from the Cooperative Institute for Research in the Atmosphere (CIRA). The authors thank Lixin Lu (CIRA) for her insight into land surface processes in the initial stages of this study, as well as Richard Johnson and Jay Ham (Colorado State University) for their insightful comments and suggestions in serving on the lead author's Master's committee. The authors also thank Toshihisa Matsui and two other anonymous reviewers, whose suggestions improved the clarity and content of the manuscript.

### References

- Alpert, P., and T. Sholokhman (Eds.) (2011), *Factor Separation in the Atmosphere: Applications and Future Prospects*, Cambridge Univ. Press, New York.
- Alpert, P., S. O. Krichak, T. N. Krishnamurti, U. Stein, and M. Tsidulko (1996), The relative roles of lateral boundaries, initial conditions, and topography in mesoscale simulations of lee cyclogenesis, *J. Appl. Meteorol.*, *35*(7), 1091–1099, doi:10.1175/1520-0450(1996)035<1091:TRROLB>2.0.CO;2.
- Andreae, M. O., and D. Rosenfeld (2008), Aerosol–cloud–precipitation interactions. Part 1. The nature and sources of cloud-active aerosols, *Earth Sci. Rev.*, *89*(1–2), 13–41, doi:10.1016/j.earscirev.2008.03.001.
- Andreae, M. O., D. Rosenfeld, P. Artaxo, A. A. Costa, G. P. Frank, K. M. Longo, and M. A. F. Silva-Dias (2004), Smoking rain clouds over the Amazon, *Science*, *303*(5662), 1337–1342, doi:10.1126/science.1092779.
- Atkins, N. T., R. M. Wakimoto, and T. M. Weckwerth (1995), Observations of the sea-breeze front during CaPE. Part II: Dual-Doppler and aircraft analysis, *Mon. Weather Rev.*, *123*(4), 944–969, doi:10.1175/1520-0493(1995)123<0944:OOTSBF>2.0.CO;2.
- Avissar, R., and D. Werth (2005), Global hydroclimatological teleconnections resulting from tropical deforestation, *J. Hydrometeorol.*, *6*(2), 134–145, doi:10.1175/JHM406.1.
- Baker, R. D., B. H. Lynn, A. Boone, W.-K. Tao, and J. Simpson (2001), The influence of soil moisture, coastline curvature, and land-breeze circulations on sea-breeze-initiated precipitation, *J. Hydrometeorol.*, *2*(2), 193–211, doi:10.1175/1525-7541(2001)002<0193:TIOSMC>2.0.CO;2.
- Balas, N., S. E. Nicholson, and D. Klotter (2007), The relationship of rainfall variability in West Central Africa to sea-surface temperature fluctuations, *Int. J. Climatol.*, *27*(10), 1335–1349, doi:10.1002/joc.1456.
- Barbaro, E., J. V.-G. de Arellano, H. G. Ouwersloot, J. S. Schröter, D. P. Donovan, and M. C. Krol (2014), Aerosols in the convective boundary layer: Shortwave radiation effects on the coupled land-atmosphere system, *J. Geophys. Res. Atmos.*, *119*, 5845–5863, doi:10.1002/2013JD021237.
- Betts, A. K. (2007), Coupling of water vapor convergence, clouds, precipitation, and land-surface processes, *J. Geophys. Res.*, *112*, D10108, doi:10.1029/2006JD008191.
- Betts, A. K. (2009), Land-surface-atmosphere coupling in observations and models, *J. Adv. Model. Earth Syst.*, *2*, 4, doi:10.3894/JAMES.2009.1.4.
- Carbone, R. E., J. W. Wilson, T. D. Keenan, and J. M. Hacker (2000), Tropical island convection in the absence of significant topography. Part I: Life cycle of diurnally forced convection, *Mon. Weather Rev.*, *128*(10), 3459–3480, doi:10.1175/1520-0493(2000)128<3459:TICITA>2.0.CO;2.
- Ciesielski, P. E., et al. (2014), Quality-controlled upper-air sounding dataset for DYNAMO/CINDY/AMIE: Development and corrections, *J. Atmos. Oceanic Tech.*, *31*(4), 741–764, doi:10.1175/JTECH-D-13-00165.1.
- Cotton, W. R., et al. (2003), RAMS 2001: Current status and future directions, *Meteorol. Atmos. Phys.*, *82*(1–4), 5–29, doi:10.1007/s00703-001-0584-9.
- Cowie, S. M., P. Knippertz, and J. H. Marsham (2013), Are vegetation-related roughness changes the cause of the recent decrease in dust emission from the Sahel?, *Geophys. Res. Lett.*, *40*, 1868–1872, doi:10.1002/grl.50273.
- Crosman, E. T., and J. D. Horel (2010), Sea and lake breezes: A review of numerical studies, *Boundary Layer Meteorol.*, *137*(1), 1–29, doi:10.1007/s10546-010-9517-9.
- Darby, L. S., R. M. Banta, and R. A. Pielke (2002), Comparisons between mesoscale model terrain sensitivity studies and Doppler lidar measurements of the sea breeze at Monterey Bay, *Mon. Weather Rev.*, *130*(12), 2813–2838, doi:10.1175/1520-0493(2002)130<2813:CBMMTS>2.0.CO;2.
- DeMott, P. J., A. J. Prenni, X. Liu, S. M. Kreidenweis, M. D. Petters, C. H. Twohy, M. S. Richardson, T. Eidhammer, and D. C. Rogers (2010), Predicting global atmospheric ice nuclei distributions and their impacts on climate, *Proc. Natl. Acad. Sci. U.S.A.*, *107*(25), 11,217–11,222, doi:10.1073/pnas.0910818107.
- Doswell, C. A. (1987), The distinction between large-scale and mesoscale contribution to severe convection: A case study example, *Weather Forecasting*, *2*(1), 3–16, doi:10.1175/1520-0434(1987)002<0003:TDBLSA>2.0.CO;2.
- Droegemeier, K. K., and R. B. Wilhelmson (1985), Three-dimensional numerical modeling of convection produced by interacting thunderstorm outflows. Part I: Control simulation and low-level moisture variations, *J. Atmos. Sci.*, *42*(22), 2381–2403, doi:10.1175/1520-0469(1985)042<2381:TDNMOC>2.0.CO;2.
- Emanuel, K. A. (1994), *Atmospheric Convection*, Oxford Univ. Press, New York.
- Fankhauser, J. C., N. A. Crook, J. Tuttle, L. J. Miller, and C. G. Wade (1995), Initiation of deep convection along boundary layer convergence lines in a semitropical environment, *Mon. Weather Rev.*, *123*(2), 291–314, doi:10.1175/1520-0493(1995)123<0291:IODCAB>2.0.CO;2.
- Feingold, G., H. Jiang, and J. Y. Harrington (2005), On smoke suppression of clouds in Amazonia, *Geophys. Res. Lett.*, *32*, L02804, doi:10.1029/2004GL021369.
- Fovell, R. G. (2005), Convective initiation ahead of the sea-breeze front, *Mon. Weather Rev.*, *133*(1), 264–278, doi:10.1175/MWR-2852.1.
- Fovell, R. G., and P. S. Dailey (2001), Numerical simulation of the interaction between the sea-breeze front and horizontal convective rolls. Part II: Alongshore ambient flow, *Mon. Weather Rev.*, *129*(8), 2057–2072, doi:10.1175/1520-0493(2001)129<2057:NSOTIB>2.0.CO;2.
- Garratt, J. R. (1993), Sensitivity of climate simulations to land-surface and atmospheric boundary-layer treatments—A review, *J. Clim.*, *6*(3), 419–448, doi:10.1175/1520-0442(1993)006<0419:SOCSTL>2.0.CO;2.
- Gero, A. F., and A. J. Pitman (2006), The impact of land cover change on a simulated storm event in the Sydney Basin, *J. Appl. Meteorol. Climatol.*, *45*(2), 283–300, doi:10.1175/JAM2337.1.
- Gu, L., D. D. Baldocchi, S. C. Wofsy, J. W. Munger, J. J. Michalsky, S. P. Urbanski, and T. A. Boden (2003), Response of a deciduous forest to the Mount Pinatubo eruption: Enhanced photosynthesis, *Science*, *299*(5615), 2035–2038, doi:10.1126/science.1078366.
- Gunthe, S. S., et al. (2009), Cloud condensation nuclei in pristine tropical rainforest air of Amazonia: Size-resolved measurements and modeling of atmospheric aerosol composition and CCN activity, *Atmos. Chem. Phys.*, *9*(19), 7551–7575, doi:10.5194/acp-9-7551-2009.
- Harrington, J. Y. (1997), The effects of radiative and microphysical processes on simulated warm and transition season Arctic stratus, PhD dissertation, 289 pp., Colo. State Univ., Fort Collins.
- Hill, G. E. (1974), Factors controlling the size and spacing of cumulus clouds as revealed by numerical experiments, *J. Atmos. Sci.*, *31*(3), 646–673, doi:10.1175/1520-0469(1974)031<0646:FCTSAS>2.0.CO;2.
- Hinrichsen, D. (1999), *Coastal Waters of the World: Trends, Threats, and Strategies*, Island Press, Washington, D. C.

- Jackson, B., S. E. Nicholson, and D. Klotter (2009), Mesoscale convective systems over western equatorial Africa and their relationship to large-scale circulation, *Mon. Weather Rev.*, *137*(4), 1272–1294, doi:10.1175/2008MWR2525.1.
- Jiang, H., and G. Feingold (2006), Effect of aerosol on warm convective clouds: Aerosol-cloud-surface flux feedbacks in a new coupled large eddy model, *J. Geophys. Res.*, *111*, D01202, doi:10.1029/2005JD006138.
- Johns, R. H., and C. A. Doswell (1992), Severe local storms forecasting, *Weather Forecasting*, *7*(4), 588–612, doi:10.1175/1520-0434(1992)007<0588:SLSF>2.0.CO;2.
- Kala, J., T. J. Lyons, D. J. Abbs, and U. S. Nair (2010), Numerical simulations of the impacts of land-cover change on a southern sea breeze in south-west Western Australia, *Boundary Layer Meteorol.*, *135*(3), 485–503, doi:10.1007/s10546-010-9486-z.
- Khain, A., D. Rosenfeld, and A. Pokrovsky (2005), Aerosol impact on the dynamics and microphysics of deep convective clouds, *Q. J. R. Meteorol. Soc.*, *131*(611), 2639–2663, doi:10.1256/qj.04.62.
- Kikuchi, K., and B. Wang (2008), Diurnal precipitation regimes in the global tropics, *J. Clim.*, *21*(11), 2680–2696, doi:10.1175/2007JCLI2051.1.
- Kingsmill, D. E. (1995), Convection initiation associated with a sea-breeze front, a gust front, and their collision, *Mon. Weather Rev.*, *123*(10), 2913–2933, doi:10.1175/1520-0493(1995)123<2913:CIAWAS>2.0.CO;2.
- Klemp, J. B., and R. B. Wilhelmson (1978), The simulation of three-dimensional convective storm dynamics, *J. Atmos. Sci.*, *35*(6), 1070–1096, doi:10.1175/1520-0469(1978)035<1070:TSOTDC>2.0.CO;2.
- Koren, I., Y. J. Kaufman, L. A. Remer, and J. V. Martins (2004), Measurement of the effect of Amazon smoke on inhibition of cloud formation, *Science*, *303*(5662), 1342–1345, doi:10.1126/science.1089424.
- Koren, I., J. V. Martins, L. A. Remer, and H. Afargan (2008), Smoke invigoration versus inhibition of clouds over the Amazon, *Science*, *321*(5891), 946–949, doi:10.1126/science.1159185.
- Kousky, V. E. (1980), Diurnal rainfall variation in northeast Brazil, *Mon. Weather Rev.*, *108*(4), 488–498, doi:10.1175/1520-0493(1980)108<0488:DRVNB>2.0.CO;2.
- Laing, A. G., R. Carbone, V. Levizzani, and J. Tuttle (2008), The propagation and diurnal cycles of deep convection in northern tropical Africa, *Q. J. Roy. Meteorol. Soc.*, *134*(630), 93–109, doi:10.1002/qj.194.
- Laing, A. G., R. E. Carbone, and V. Levizzani (2011), Cycles and propagation of deep convection over equatorial Africa, *Mon. Weather Rev.*, *139*(9), 2832–2853, doi:10.1175/2011MWR3500.1.
- Liebmann, B., I. Bladé, G. N. Kiladis, L. M. V. Carvalho, G. B. Senay, D. Allured, S. Leroux, and C. Funk (2012), Seasonality of African precipitation from 1996 to 2009, *J. Clim.*, *25*(12), 4304–4322, doi:10.1175/JCLI-D-11-00157.1.
- Lilly, D. K. (1962), On the numerical simulation of buoyant convection, *Tellus*, *14*(2), 148–172, doi:10.1111/j.2153-3490.1962.tb00128.x.
- Lin, J. C., T. Matsui, R. A. Pielke, and C. Kummerow (2006), Effects of biomass-burning-derived aerosols on precipitation and clouds in the Amazon Basin: A satellite-based empirical study, *J. Geophys. Res.*, *111*, D19204, doi:10.1029/2005JD006884.
- Lu, L., A. S. Denning, M. A. da Silva-Dias, P. da Silva-Dias, M. Longo, S. R. Freitas, and S. Saatchi (2005), Mesoscale circulations and atmospheric CO<sub>2</sub> variations in the Tapajós Region, Pará, Brazil, *J. Geophys. Res.*, *110*, D21102, doi:10.1029/2004JD005757.
- Mahmood, R., et al. (2014), Land cover changes and their biogeophysical effects on climate, *Int. J. Climatol.*, *34*(4), 929–953, doi:10.1002/joc.3736.
- Marshall, C. H., R. A. Pielke, L. T. Steyaert, and D. A. Willard (2004), The impact of anthropogenic land-cover change on the Florida peninsula sea breezes and warm season sensible weather, *Mon. Weather Rev.*, *132*(1), 28–52.
- Martin, S. T., et al. (2010), Sources and properties of Amazonian aerosol particles, *Rev. Geophys.*, *48*, RG2002, doi:10.1029/2008RG000280.
- Matsui, T., A. Beltrán-Przekurat, D. Niyogi, R. A. Pielke, and M. Coughenour (2008), Aerosol light scattering effect on terrestrial plant productivity and energy fluxes over the eastern United States, *J. Geophys. Res.*, *113*, D14514, doi:10.1029/2007JD009658.
- McCollum, J. R., A. Gruber, and M. B. Ba (2000), Discrepancy between gauges and satellite estimates of rainfall in equatorial Africa, *J. Appl. Meteorol.*, *39*(5), 666–679, doi:10.1175/1520-0450-39.5.666.
- Meyers, M. P., R. L. Walko, J. Y. Harrington, and W. R. Cotton (1997), New RAMS cloud microphysics parameterization. Part II: The two-moment scheme, *Atmos. Res.*, *45*(1), 3–39, doi:10.1016/S0169-8095(97)00018-5.
- Miao, J.-F., L. J. M. Kroon, J. Vila-Guerau de Arellano, and A. A. M. Holtslag (2003), Impacts of topography and land degradation on the sea breeze over eastern Spain, *Meteorol. Atmos. Phys.*, *84*(3–4), 157–170, doi:10.1007/s00703-002-0579-1.
- Mohr, K. I., and E. J. Zipser (1996a), Defining mesoscale convective systems by their 85-GHz ice-scattering signatures, *Bull. Am. Meteorol. Soc.*, *77*(6), 1179–1189, doi:10.1175/1520-0477(1996)077<1179:DMCSBT>2.0.CO;2.
- Mohr, K. I., and E. J. Zipser (1996b), Mesoscale convective systems defined by their 85-GHz ice scattering signature: Size and intensity comparison over tropical oceans and continents, *Mon. Weather Rev.*, *124*(11), 2417–2437, doi:10.1175/1520-0493(1996)124<2417:MCSDBT>2.0.CO;2.
- Mohr, K. I., J. S. Famiglietti, and E. J. Zipser (1999), The contribution to tropical rainfall with respect to convective system type, size, and intensity estimated from the 85-GHz ice-scattering signature, *J. Appl. Meteorol.*, *38*(5), 596–606, doi:10.1175/1520-0450(1999)038<0596:TCTTRW>2.0.CO;2.
- Nesbitt, S., and E. Zipser (2003), The diurnal cycle of rainfall and convective intensity according to three years of TRMM measurements, *J. Clim.*, *16*(10), 1456–1475.
- Nesbitt, S. W., R. Cifelli, and S. A. Rutledge (2006), Storm morphology and rainfall characteristics of TRMM precipitation features, *Mon. Weather Rev.*, *134*(10), 2702–2721, doi:10.1175/MWR3200.1.
- O'Brien, K. L. (2000), Upscaling tropical deforestation: Implications for climate change, *Clim. Change*, *44*(3), 311–329, doi:10.1023/A:1005531521525.
- Petersen, W. A., and S. A. Rutledge (1998), On the relationship between cloud-to-ground lightning and convective rainfall, *J. Geophys. Res.*, *103*(D12), 14,025, doi:10.1029/97JD02064.
- Petersen, W. A., and S. A. Rutledge (2001), Regional variability in tropical convection: Observations from TRMM, *J. Clim.*, *14*(17), 3566–3586, doi:10.1175/1520-0442(2001)014<3566:RVITCO>2.0.CO;2.
- Physick, W. L. (1980), Numerical experiments on the inland penetration of the sea breeze, *Q. J. Roy. Meteorol. Soc.*, *106*(450), 735–746, doi:10.1002/qj.49710645007.
- Pielke, R. A., J. Adegoke, A. Beltrán-Przekurat, C. A. Hiemstra, J. Lin, U. S. Nair, D. Niyogi, and T. E. Nobis (2007), An overview of regional land-use and land-cover impacts on rainfall, *Tellus B*, *59*(3), 587–601, doi:10.1111/j.1600-0889.2007.00251.x.
- Ramos da Silva, R., and R. Avissar (2006), The hydrometeorology of a deforested region of the Amazon Basin, *J. Hydrometeorol.*, *7*(5), 1028–1042, doi:10.1175/JHM537.1.
- Riehl, H., and J. S. Malkus (1958), On the heat balance in the equatorial trough zone, *Geophysica*, *6*(3–4), 503–538.
- Roberts, G. C., M. O. Andreae, J. Zhou, and P. Artaxo (2001), Cloud condensation nuclei in the Amazon Basin: “Marine” conditions over a continent?, *Geophys. Res. Lett.*, *28*(14), 2807–2810, doi:10.1029/2000GL012585.
- Robinson, F. J., M. D. Patterson, and S. C. Sherwood (2013), A numerical modeling study of the propagation of idealized sea-breeze density currents, *J. Atmos. Sci.*, *70*(2), 653–668, doi:10.1175/JAS-D-12-0113.1.
- Rodell, M., et al. (2004), The global land data assimilation system, *Bull. Am. Meteorol. Soc.*, *85*(3), 381–394, doi:10.1175/BAMS-85-3-381.

- Saad, S. I., H. R. da Rocha, M. A. F. Silva Dias, and R. Rosolem (2010), Can the deforestation breeze change the rainfall in Amazonia? A case study for the BR-163 highway region, *Earth Interact.*, *14*(18), 1–25, doi:10.1175/2010EI351.1.
- Saleeby, S. M., and W. R. Cotton (2004), A large-droplet mode and prognostic number concentration of cloud droplets in the Colorado State University Regional Atmospheric Modeling System (RAMS). Part I: Module descriptions and supercell test simulations, *J. Appl. Meteorol.*, *43*(1), 182–195, doi:10.1175/1520-0450(2004)043<0182:ALMAPN>2.0.CO;2.
- Saleeby, S. M., and W. R. Cotton (2008), A binned approach to cloud-droplet riming implemented in a bulk microphysics model, *J. Appl. Meteorol. Climatol.*, *47*(2), 694–703, doi:10.1175/2007JAMC1664.1.
- Saleeby, S. M., and S. C. van den Heever (2013), Developments in the CSU-RAMS aerosol model: Emissions, nucleation, regeneration, deposition, and radiation, *J. Appl. Meteorol. Climatol.*, *52*(12), 2601–2622, doi:10.1175/JAMC-D-12-0312.1.
- Seigel, R. B., S. C. van den Heever, and S. M. Saleeby (2013), Mineral dust indirect effects and cloud radiative feedbacks of a simulated idealized nocturnal squall line, *Atmos. Chem. Phys.*, *13*(8), 4467–4485, doi:10.5194/acp-13-4467-2013.
- Smagorinsky, J. (1963), General circulation experiments with the primitive equations I. The basic experiment, *Mon. Weather Rev.*, *91*(3), 99–164, doi:10.1175/1520-0493(1963)091<0099:GCEWTP>2.3.CO;2.
- Stein, U., and P. Alpert (1993), Factor separation in numerical simulations, *J. Atmos. Sci.*, *50*(14), 2107–2115, doi:10.1175/1520-0469(1993)050<2107:FSINS>2.0.CO;2.
- Taylor, C. M., R. A. M. de Jeu, F. Guichard, P. P. Harris, and W. A. Dorigo (2012), Afternoon rain more likely over drier soils, *Nature*, *489*(7416), 423–6, doi:10.1038/nature11377.
- Tompkins, A. M. (2001), Organization of tropical convection in low vertical wind shears: The role of cold pools, *J. Atmos. Sci.*, *58*(13), 1650–1672, doi:10.1175/1520-0469(2001)058<1650:OOTCIL>2.0.CO;2.
- van den Heever, S. C., G. G. Carrió, W. R. Cotton, P. J. DeMott, and A. J. Prenni (2006), Impacts of nucleating aerosol on Florida storms. Part I: Mesoscale simulations, *J. Atmos. Sci.*, *63*(7), 1752–1775, doi:10.1175/JAS3713.1.
- Vondou, D. A., A. Nzeukou, and F. M. Kamga (2010), Diurnal cycle of convective activity over the west of Central Africa based on Meteosat images, *Int. J. Appl. Earth Obs. Geoinf.*, *12*, S58–S62, doi:10.1016/j.jag.2009.09.011.
- Wakimoto, R. M., and N. T. Atkins (1994), Observations of the sea-breeze front during CaPE. Part I: Single-Doppler, satellite, and cloud photogrammetry analysis, *Mon. Weather Rev.*, *122*(6), 1092–1114, doi:10.1175/1520-0493(1994)122<1092:OOTSBF>2.0.CO;2.
- Walko, R. L., W. R. Cotton, M. P. Meyers, and J. Y. Harrington (1995), New RAMS cloud microphysics parameterization. Part I: The single-moment scheme, *Atmos. Res.*, *38*(1–4), 29–62, doi:10.1016/0169-8095(94)00087-T.
- Walko, R. L., et al. (2000), Coupled atmosphere–biophysics–hydrology models for environmental modeling, *J. Appl. Meteorol.*, *39*(6), 931–944, doi:10.1175/1520-0450(2000)039<0931:CABHMF>2.0.CO;2.
- Wilson, J. W., and D. L. Megenhardt (1997), Thunderstorm initiation, organization, and lifetime associated with Florida boundary layer convergence lines, *Mon. Weather Rev.*, *125*(7), 1507–1525, doi:10.1175/1520-0493(1997)125<1507:TIOALA>2.0.CO;2.
- Xue, H., and G. Feingold (2006), Large-eddy simulations of trade wind cumuli: Investigation of aerosol indirect effects, *J. Atmos. Sci.*, *63*(6), 1605–1622, doi:10.1175/JAS3706.1.
- Yang, G.-Y., and J. Slingo (2001), The diurnal cycle in the tropics, *Mon. Weather Rev.*, *129*(4), 784–801, doi:10.1175/1520-0493(2001)129<0784:TDCITT>2.0.CO;2.
- Yu, H., S. C. Liu, and R. E. Dickinson (2002), Radiative effects of aerosols on the evolution of the atmospheric boundary layer, *J. Geophys. Res.*, *107*(D12), 4142, doi:10.1029/2001JD000754.
- Zhang, Y., R. Fu, H. Yu, R. E. Dickinson, R. N. Juarez, M. Chin, and H. Wang (2008), A regional climate model study of how biomass burning aerosol impacts land-atmosphere interactions over the Amazon, *J. Geophys. Res.*, *113*, D14S15, doi:10.1029/2007JD009449.
- Zipser, E. J., C. Liu, D. J. Cecil, S. W. Nesbitt, and D. P. Yorty (2006), Where are the most intense thunderstorms on Earth?, *Bull. Am. Meteorol. Soc.*, *87*(8), 1057–1071, doi:10.1175/BAMS-87-8-1057.